

QUANTUM CONTROL FOR TIME-DEPENDENT NOISE

A Thesis
Presented to
The Academic Faculty

by

Chingiz Kabytayev

In Partial Fulfillment
of the Requirements for the Degree
Doctor of Philosophy in the
School of Physics

Georgia Institute of Technology
August 2015

Copyright © 2015 by Chingiz Kabytayev

QUANTUM CONTROL FOR TIME-DEPENDENT NOISE

Approved by:

Professor Thomas Orlando,
Committee Chair
School of Chemistry and Biochemistry
Georgia Institute of Technology

Professor Kenneth R. Brown, Advisor
School of Chemistry and Biochemistry
Georgia Institute of Technology

Professor Michael S. Chapman
School of Physics
Georgia Institute of Technology

Professor T. A. Brian Kennedy
School of Physics
Georgia Institute of Technology

Professor Michael Pustilnik
School of Physics
Georgia Institute of Technology

Date Approved: April 29, 2015

To the memory of my late grandfather,

Bolat Bekenov

ACKNOWLEDGEMENTS

Graduate school has been the most interesting and most challenging stage of my life so far. I would like to recognize people who have always supported and encouraged me during these years. First of all, I express my special appreciation to my advisor, Professor Kenneth R. Brown, for his continuous support, professionalism, enthusiasm, patience and extraordinary talent to teach people. He has an immense knowledge not only on the research topics relevant to the work, but also a broad and deep insight about various phenomena which were always exciting to learn about.

I would like to thank the committee members, Professor Michael Chapman, Professor Brian Kennedy, Professor Thomas Orlando and Professor Michael Pustilnik, for their valuable feedback and their time.

The significant part of this work has been done together with our collaborators, and I would like to acknowledge all of them. I appreciate the guidance of Professor Lorenza Viola, who has been an amazing supervisor during my visits to her research group at Dartmouth College. I am really thankful to Dr. Kaveh Khodjasteh for teaching me a number of practical tricks that have made my research work more productive. I also would like to thank Todd Green and Professor Michael Biercuk from Sydney University as well as Emily Mount and Professor Jungsang Kim from Duke University for an effective collaboration.

It has been amazing to work next to my colleagues in the Brown lab. I have been fortunate to know all of them and I would like to thank the former members, Craig Clark, James Goeders, True Merrill, Grahame Vittorini (for his *loud* and sharp sense of humor), Yu Tomita, Ted Chang, Yon Choi, Mason Bogue, and the current members, Mauricio Gutiérrez, JB Khanyile, Rick Shu, Colin Trout, Rene Rugango,

Smitha Janardan, Aaron Calvin and Harrison Ansley.

Special thanks go to all of my family members, my grandparents and parents. I especially thank my aunt Saltanat Kalimoldayeva and my uncle Maksat Kalimoldayev for their extensive support.

Finally, I am thankful to my fiancée, Aliya Mukazhanova, who has always inspired me to move forward.

TABLE OF CONTENTS

DEDICATION	iii
ACKNOWLEDGEMENTS	iv
LIST OF TABLES	viii
LIST OF FIGURES	ix
SUMMARY	xiii
I INTRODUCTION	1
1.1 Quantum control in the presence of noise fields	1
1.2 Organization of the thesis	3
II QUANTUM CONTROL	5
2.1 Fundamentals of quantum control	5
2.1.1 Controllability	6
2.1.2 Qubit control for quantum computing	7
2.1.3 Bloch-vector rotations	9
2.1.4 Imperfections in control	11
2.1.5 Time-dependent noise	13
2.2 Theoretical framework for time-dependent noise	15
2.2.1 Time-dependent error model for control protocols	15
2.2.2 Performance measure and filter-transfer functions	18
2.3 Optimal control	21
2.3.1 Optimal control for state-to-state transitions	22
2.3.2 Optimal control for the evolution operator	24
2.3.3 Optimization methods	26
2.4 Conclusion	33
III COMPOSITE PULSE SEQUENCES IN THE PRESENCE OF TIME-DEPENDENT NOISE	34
3.1 Composite Pulses	35

3.2	Robustness of composite pulses to time-dependent noise	35
3.2.1	Analytical results	35
3.2.2	Geometric picture	37
3.2.3	DC limit	41
3.2.4	Comparison with numerical results	42
3.3	Trapezoidal pulses	48
3.4	Conclusion	50
IV	OPTIMIZED PULSE SEQUENCES THAT ACT AS NOTCH FIL-	
	TERS	51
4.1	Noise model	52
4.2	Control of amplitude noise	54
4.3	Control of detuning noise	55
4.3.1	Objective function and Optimization procedure	57
4.4	Results	59
4.4.1	Amplitude noise	59
4.4.2	Detuning noise	61
4.5	Conclusion	61
V	COMPOSITE PULSES FOR SINGLE-QUBIT GATES IN A SUR-	
	FACE ELECTRODE ION TRAP	62
5.1	Experimental methods	62
5.2	Randomized benchmarking	65
5.3	Experimental results and numeric simulation	67
5.4	Conclusion	67
VI	CONCLUSION	70
	APPENDIX A — NUMERICAL NOISE SIMULATION	71
	REFERENCES	73

LIST OF TABLES

1	CP sequences correcting the target rotation $R(\theta, 0)$ against different error models [1, 2]. Here, $\phi_1 = \cos^{-1}(-\theta/4\pi)$, $k = \arcsin[\sin(\theta/2)/2]$, $\alpha = 2\pi + \theta/2$, a : amplitude noise; d : detuning noise; s : simultaneous amplitude and detuning noise [see text]. For the DCG sequence [3, 4], $\Omega_1 = \Omega$, $0 \leq t < t_1 \equiv \tau/4$; $\Omega_2 = \Omega/2$, $t_1 \leq t < t_2 \equiv 3\tau/4$; $\Omega_3 = \Omega$, $t_2 \leq t < t_3 \equiv \tau$	36
2	The Clifford group gates written as the physical gates applied. . . .	69

LIST OF FIGURES

1	Bloch sphere representation.	8
2	Examples of Bloch vector rotations generated by propagator of Eq. (13). In the case of constant Rabi frequency, rotation angle, θ , is defined through $\theta = \Omega\tau$. Rotation axis is determined by phase ϕ . In all three examples, the initial state is $ 0\rangle$ (gray dashed vector).	11
3	Graphical demonstration of amplitude (Eq. (15)), detuning (Eq. (18)) and simultaneous (Eq. (17)) error in the case of intended y -rotation by angle $\theta = \pi/2$. Ideal evolution is represented by a blue color with final state denoted by a blue dashed-dot vector along x -axis. Imperfect rotation is denoted by red color. In all three cases the chosen initial state is $ 0\rangle$ (denoted by gray dashed vector). The error parameters are chosen to be large ($\epsilon = \delta = 0.2$) to clearly demonstrate the effect of noise.	14
4	Example of filter-transfer function (top) and spectral density (bottom) that can be used for estimating performance of a control operation. Fidelity loss is estimated according to Eq. (23) as an overlap integral of these two functions in a frequency domain within particular limits (in this example it is denoted by a shaded area).	20
5	Basic flow for gradient ascent pulse engineering (GRAPE) algorithm. See text for details.	29
6	Basic flow for Simulated Annealing algorithm. In accordance with thermodynamical analogy, x plays a role of a system state (described by set of controls $u_k(j)$); objective function Φ_0 is an effective energy of system that we need to minimize; $T(t)$ is an effective temperature at time t ; $\Delta\Phi_0 = \Phi_0(u_k(j)) - \Phi_0(u_k(i))$. Termination conditions are typically based on a low temperature threshold or certain number of repetitions.	31
7	First 8 Walsh functions in Paley ordering	32
8	Example of various shapes for spectral density for three different values of a roll-off knee, ω_b	37

9	Top: FFs as a function of dimensionless frequency for amplitude [Panel a)], and detuning noise [Panel b)]. A target rotation angle $\theta = \pi$ is used for all sequences. Bottom: Performance of CP sequences in the presence of constant power amplitude [Panel c)] and detuning noise [Panel d)] with $1/f$ Gaussian noise spectrum and $1/f^2$ roll-off, Eq. (59). Spectrum parameters: $A_a = A_d \equiv A = 2.07 \cdot 10^9 / [\log(\omega_b/\omega_{\min}) + 1 - (\omega_b/\omega_{\max})]$ (rad/s) ³ /Hz, where ω_b is the knee of the roll-off; $\omega_{\min} = 2\pi$ rad/s, $\omega_{\max} = 4.5 \cdot 10^9$ rad/s. Control amplitude: $\Omega = 1.5 \cdot 10^6$ rad/s. Numerical simulation involves discretization of the continuous noise functions $\beta_\mu(t)$, calculating a single instance of $U(\tau, 0)$ and a single value for fidelity, and averaging over N noise realizations. We employ the Karhunen-Loeve filter [5] to simulate discrete noise in the Gaussian limit [6]. Analytical lines representing the fidelity loss calculated by the FF approach [Eq. (68), in color] and by the DC limit approach [Eq. (58), gray] are plotted. The DC limit for BB1 and CORPSE are below the bounds of the plot at $1 - \mathcal{F} = 3.9 \times 10^{-9}$ and $1 - \mathcal{F} = 3.0 \times 10^{-9}$, respectively	38
10	Geometric picture for first- vs. second-order amplitude-error CPs. The axes represent Cartesian x and y , indicating the rotation axes of the different segments [see text]. The initial rotation is about the x -axis, indicated by the horizontal line, with corrections about different axes conducted subsequently. Returning to the origin indicates suppression of error, with two different time-domain elements of the FF being indicated by color (dashed green/solid red).	40
11	(a) Distribution of an angle of error rotation, ε (see text), based on 1000 samples of numeric noise realizations for primitive X -gate. (b) Distribution of deviations of fidelity loss for primitive X -gate. Black bars correspond to numeric calculations and red dashed line corresponds to Eq. (60).	44
12	Distributions for fidelity loss deviations based on 1000 samples of numeric noise realizations for BB1 and SK1 CP sequences.	45
13	FFs as a function of dimensionless frequency for amplitude error [Panel a)] and detuning error [Panel b)] for concatenated CP sequences Reduced CinSK and Reduced CinBB. Unlike SK1, BB1, CORPSE, and DCG (see Fig. 9), these FFs scale as ω^4 for both errors.	46
14	Performance of CPs under simultaneous amplitude and detuning noise, as a function of dimensionless frequency roll-off from $1/f$ to a $1/f^2$ spectral density, ω_b^a and ω_b^d , respectively. Spectrum and control parameters as in Fig. 9. Analytical results for fidelity loss. For each point the FF and DC limit calculations are compared and the larger fidelity loss value is plotted.	47

15	Performance of Reduced CinBB under simultaneous amplitude and detuning noise, as a function of dimensionless frequency roll-off from $1/f$ to a $1/f^2$ spectral density, ω_b^a and ω_b^d , respectively. Spectrum and control parameters as in Fig. 9. Analytical (FF: green surface, DC-limit: gray surface) and numerical results (green circles and mesh) for Reduced CinBB vs. analytical (DC-limit: blue surface) and numerical results (black diamonds) for a primitive pulse.	47
16	FFs as a function of dimensionless frequency for SK1 [Panel a)] and BB1 [Panel c)] in the presence of multiplicative amplitude noise and for CORPSE [Panel b)] and DCG [Panel d)] in the presence of detuning noise. The CPs are constructed from trapezoidal pulses with ramp time r in units of π/Ω	49
17	Example of considered power spectrum of Eq. (61) formed by Gaussian-shape peak with $\omega_0/\Omega \simeq 0.44$ (Eq. (62)) and $1/f$ background with a roll-off to $1/f^2$	53
18	Example of noise trajectories for $\omega_0/\Omega \simeq 0.44$ corresponding to the spectrum of Eq. (61).	53
19	Top: FFs as a function of dimensionless frequency. Vertical dashed lines indicate target values of ω_0 for which control protocols based on Eq. (65) [Panel a)] and based on Eq. (66) [Panel c)] were synthesized. Bottom: Performance of quantum control protocols as a function of parameter ω_0/Ω for a Gaussian spectral peak including control protocols based on Eq. (65) [Panel b)] and based on Eq. (66) [Panel d)]. Analytical fidelity loss computed by the FF approach (lines) is compared to numerical simulations (markers).	55
20	(a) FFs as a function of dimensionless frequency. Vertical dashed lines indicate target values of ω_0 for which OCP ₁ and OCP ₂ were synthesized. (b) Performance of quantum control protocols as a function of central frequency ω_0/Ω for a Gaussian peak in detuning spectrum. Analytical fidelity loss based on the FF approach (lines) is compared to numerical simulation (markers). Spectrum parameters: (c) Amplitude profile for OCP ₁ synthesized from Walsh functions (d) Amplitude profile for OCP ₂ . Diagonal-line pattern of 3rd and 6th pulse corresponds to the rotation phase $\phi_1 = \phi_8 = \pi$ which equals 0 elsewhere.	56
21	Performance of GRAPE pulse sequences optimized for $\omega_0 \simeq 0.44$ with 5-pulse structure (a) and 10-pulse structure (b). Control power profiles are given on panels (c) and (d), respectively. Dashed Horizontal lines denote 'slow' π -pulse. Fidelity loss for the F_1 -type pulse sequence (Fig 19) is given for comparison.	60
22	Relevant energy levels used in the $^{171}\text{Yb}^+$ ion. Adapted from [7]. . . .	64

23	Relevant optical frequency combs. Adapted from [7].	64
24	Single qubit gate error degradation with systematic amplitude error. .	68

SUMMARY

The main obstacles to implementing ideal quantum operations are unwanted interactions of quantum systems with the environment and noise in control fields. This problem can be tackled by methods of quantum control. Among these methods are composite pulse (CP) sequences which have long been employed in nuclear magnetic resonance (NMR) to mitigate the effects of systematic errors in the control. CP sequences were initially developed to correct for static but otherwise unknown errors in the amplitude or frequency of the driving field. One of the challenges to the systematic incorporation of these control protocols into practical quantum information systems remains the limited understanding of CP performance in the presence of time-dependent noise. Treating the influence of time-dependent noise processes on quantum control operations has been facilitated by recent advances in dynamical error suppression based on open-loop Hamiltonian engineering. These approaches provide a general framework for understanding and mitigating non-Markovian time-dependent noise in a finite-dimensional open quantum system. In particular, arbitrary single-qubit control characteristics may be captured quantitatively in filter-transfer functions (FF) using methods of spectral overlap in the frequency domain. In this thesis work, we present a systematic study of control pulse sequences in the presence of time-dependent noise. We use a combination of analytic formulations based on FFs and numerical simulations to demonstrate that CPs are able to effectively suppress control errors caused by time-dependent processes possessing realistic noise power spectra. We provide a geometric interpretation of CP performance under time-dependent amplitude noise, further linking the FF formalism with known techniques in CP construction. We also develop new optimized pulse sequences that act as notch

filters for time-dependent noise. These high-fidelity control protocols effectively suppress errors from the noise sources with sharp features in spectral densities and can be used practically on various quantum architectures. We also present our work on simulation of randomized benchmarking protocols and CPs that have been used experimentally by our collaborators to measure gate errors.

CHAPTER I

INTRODUCTION

Employing coherence properties of electromagnetic fields in order to steer a quantum system to a desired target state or particular dynamical behavior forms a basis for the field of quantum control of light and matter. Recent developments in this area indicate the beginnings of a new era of technology, technology that is fully based on the unique laws of quantum mechanics. Due to the rise of this “second quantum revolution” [8] there will be demand of a new and advanced quantum engineering methodologies. At the present time, this new branch of engineering associated with quantum technologies includes activities ranging from laboratory design of top-notch electronic devices and advanced control system, to theoretical developments that adopt results of classical control theory to better understand quantum-mechanical systems.

Although, many original ideas of quantum control were developed in the community of physical chemistry [9], the field has grown to a number of various applications including NMR, non-linear spectroscopy, ultra-cold physics, atto-second science, quantum computing and quantum entanglement in complex systems [10, 11, 12, 13, 9, 14, 15, 16].

1.1 Quantum control in the presence of noise fields

High-fidelity control of quantum systems is limited by unwanted interactions with the environment and imperfections in the applied control fields. Composite pulse (CP) sequences have long been employed in nuclear magnetic resonance (NMR) to mitigate the effects of systematic errors in the control [17, 18, 19, 1]. Initially developed to tackle static but otherwise unknown errors in the amplitude or frequency of the driving

field, CPs are expressed as the composition of rotations. CPs have been recently extended to handle multiple error sources using symmetry [20, 21] and concatenation [22, 2] and to provide efficient high-order error suppression by optimized design [23]. These capabilities have made CPs broadly attractive in laboratory quantum systems, including experimental platforms based on atomic [24, 25, 26, 27, 28, 29] and solid-state qubits [30, 31, 32, 33].

Despite these advances, an outstanding challenge to the systematic incorporation of CPs into practical quantum information systems remains the limited understanding of CP performance in the presence of *time-dependent* noise. This is in contrast to optimal control approaches for gate synthesis, where the presence of time-dependent noise is typically assumed in the control design, see e.g. Refs. [34, 35, 36]. Previous studies for CPs have examined a restricted set of time-dependent fluctuations in the control including the numeric characterization of decoherence due to random-telegraph noise in the qubit frequency [37], the effect of stochastic fluctuations in the phase of the control [38], and the effect of $1/f^\alpha$ noise for singlet-triplet spin qubits [39].

Treating the influence of time-dependent noise processes on quantum control operations beyond these limited examples has been facilitated by recent advances in dynamical error suppression based on open-loop Hamiltonian engineering [40, 41, 3, 42, 4]. These approaches provide a general framework for understanding and mitigating non-Markovian time-dependent noise in a finite-dimensional open quantum system due to either uncontrolled couplings to the environment or a variety of control errors. In particular, both dynamical decoupling [40, 41, 43] and dynamically corrected gates (DCGs) [3, 44, 35] are able to perturbatively reduce the effects of classical as well as quantum noise sources, provided that the correlation time scale of the noise is sufficiently long compared to the control time scale at which the noise is “coherently averaged out”. These characteristics may be captured quantitatively in filter-transfer

functions (FF henceforth) for arbitrary single-qubit control using methods of spectral overlap in the frequency domain [45, 4]. The resulting approach allows for prediction of the leading-order contribution to fidelity loss, and has been applied to the study of both dynamically protected memory [46, 47] and nontrivial quantum logic operations [48, 4] with results borne out through a variety of experiments [49, 50].

1.2 Organization of the thesis

The thesis is organized as follows. In Chapter 2 we introduce the basics of quantum control theory. Particularly, we consider the role of quantum control for quantum computing, and we also focus on a brief overview of optimal quantum control methods. Chapter 3 discusses our work on robustness of composite pulses to time-dependent noise [51]. We employ a combination of analytic formulations based on filter-transfer functions and numerical simulations to demonstrate that composite pulses effectively suppress time-dependent control errors with fluctuations as fast as $\sim 10\%$ of the Rabi frequency. We also present a geometric interpretation amplitude-noise filter function. Chapter 4 introduces our recent work on designing new optimized pulse sequences that act as notch filters. These pulse sequences effectively correct for the noise with sharp spectral features. As an example we consider a strong Gaussian-shaped peak on top of background noise with a power-law spectrum. Optimization procedures discussed in Chapter 2 provide control sequences which demonstrate high performance for a given noise model. Furthermore, the first-order filter-transfer functions yields insight into the pulse robustness with respect to changes in the position of the Gaussian peak. Finally, Chapter 4 describes our work [7] in collaboration with Duke University. It introduces our numeric simulations and experimental work of our collaborators on error compensation of single-qubit gates in a surface electrode ion trap using composite pulses. In this work among other results recently developed compact palindromic composite pulse sequences [23] have been shown to be effective

against high-amplitude errors. We also discuss randomized benchmarking protocols that have been used to measure the average error per gate.

CHAPTER II

QUANTUM CONTROL

2.1 *Fundamentals of quantum control*

In the last few decades there have been a growing interest in development of applications of quantum mechanical systems including quantum information and computation, cold atoms, control of chemical reactions, and quantum metrology [10, 11, 12, 13, 9, 14, 15, 16]. Accurate manipulation of quantum systems is crucial for these applications. In many cases, this is related to the capability of shaping electromagnetic field in an arbitrary way as many control problems can be treated as the interaction between quantum object and a classical electromagnetic field. Many quantum control experiments adopt this semiclassical approach. Quantum control is based on classical control theory and this adoption leads to new approaches to explore quantum physics [52].

In control theory, a finite dimensional control system is typically described by the set of ordinary differential equations of the form

$$\dot{\mathbf{x}} = f(t, \mathbf{x}, \mathbf{u}), \quad (1)$$

where \mathbf{x} is the state of the system and \mathbf{u} represents the set of possible control variables, $\mathbf{u} = (u_1(t), u_2(t), \dots, u_n(t))$, which modulate the dynamical response of a state \mathbf{x} .

In quantum control systems, the dynamics of the state $|\psi\rangle$ of quantum system is governed by the *Schrödinger equation* (here and elsewhere in this work we assume that $\hbar \equiv 1$)

$$i \frac{d|\psi\rangle}{dt} = H(u(t))|\psi\rangle, \quad (2)$$

where $H(u(t))$ is the Hamiltonian, a linear Hermitian operator on the same Hilbert

space \mathcal{H} , where $|\psi\rangle$ is defined. From a control perspective, $H(u(t))$ is a function of a control $u = u(t)$ which models the external manipulation on the quantum object. If $|\psi_0\rangle$ is the initial state the solution of 2 can be written as

$$|\psi\rangle = U(t)|\psi_0\rangle. \quad (3)$$

Here the propagator $U(t)$ is the solution of the *Schrödinger operator equation*

$$i\dot{U}(t) = H(u(t))U(t), \quad (4)$$

$$U(0) = 1$$

We can consider $U(t)$ as the object of control and this choice would be quite natural for quantum computing, as the matrix $U(t)$ represents the *operation* or *gate* which is acting on a state of qubits. In quantum computing, synthesizing a unitary gate $U(t)$ is more important than achieving a particular state. Therefore, in this thesis we concentrate mostly on this control setting.

The operator $U(t)$ is defined in the Lie group of n -dimensional unitary matrices, where n is the dimension of the system ($n = 2$ for a single qubit) [16]. In practice it is often possible to write down Hamiltonian in the following form

$$H(u) = H_0 + \sum_k H_k u_k. \quad (5)$$

In this bilinear representation, H_0 is a drift Hamiltonian that cannot be controlled explicitly and $\{u_k\}$ are components that define a magnitude of control along respective Hermitian operators $\{H_1, H_2, \dots, H_p\}$. Typically in the following chapters we omit a constant term H_0 by shifting to an interaction picture.

2.1.1 Controllability

One of the fundamental issues in quantum control theory is related to controllability of quantum system [16, 15]. In the case of Eq. 4 it is a question whether a desired unitary matrix \bar{U} can be reached by changing the control u belonging to a space of

functions $\bar{\mathcal{U}}$. All possible matrices that can be obtained at time T form the *reachable set* $\mathcal{R}(T)$ corresponding to that time. If $U(t, u)$ is the solution of Eq. 4, $\mathcal{R}(T)$ is the set of all unitary matrices \bar{U} such that $U(T, u) = \bar{U}$ for some control $u \in \bar{\mathcal{U}}$. Analogously, one can define the *reachable set at time T* , $\mathcal{R}(\leq T) := \cup_{0 \leq t \leq T} \mathcal{R}(t)$, and the *reachable set*, $\mathcal{R} := \cup_{T \geq 0} \mathcal{R}(t)$.

The system Eq. (4) is defined to be *controllable* if any arbitrary unitary matrix is in the reachable set. The question of controllability is practically important for the universality of quantum computation. In the case of finite dimensional quantum systems (such as qubits) it is possible to derive the controllability criteria from the structure of corresponding Lie groups and Lie algebras. The advantage of this method is that it can provide a straightforward mathematical treatment and a geometric interpretation.

In fact, reachable state \mathcal{R} is a *Lie group* - a group with additional differentiable structure [53]. One can observe that \mathcal{R} is a semigroup noting that a state $U_2 \cdot U_1$ can be reached by concatenating controls u_1 and u_2 corresponding to states U_2 and U_1 respectively [16, 53].

2.1.2 Qubit control for quantum computing

The quantum state of a two-level system, or qubit, can be described as a superposition of two basis states, $|\psi\rangle = c_0|0\rangle + c_1|1\rangle$, with normalization condition $|c_0|^2 + |c_1|^2 = 1$ [54]. Geometrically, this state is represented as a unit vector on a Bloch sphere (Fig. 1), uniquely specified by two angles, θ and ϕ (here we neglect an unobservable global phase factor $e^{i\gamma}$):

$$|\psi\rangle = \cos\left(\frac{\theta}{2}\right)|0\rangle + e^{i\phi}\sin\left(\frac{\theta}{2}\right)|1\rangle. \quad (6)$$

In quantum information a qubit plays a role similar to which a classical bit plays in computer science. Namely, information is encoded in a state of two-level system.

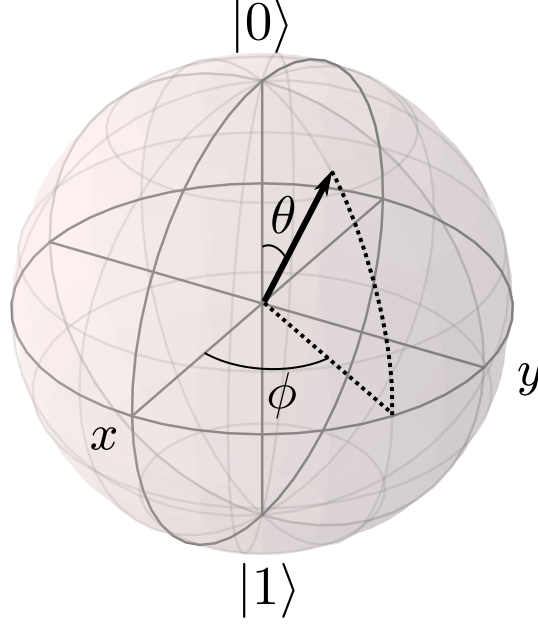


Figure 1: Bloch sphere representation.

One of the great differences between classical and quantum information is that the qubit can exist in a linear superposition of two states (Eq. (6)).

In a vector or matrix form orthogonal basis states $|0\rangle$ and $|1\rangle$ can be written as column vectors

$$|0\rangle = \begin{pmatrix} 1 \\ 0 \end{pmatrix}; \quad |1\rangle = \begin{pmatrix} 0 \\ 1 \end{pmatrix}. \quad (7)$$

The core of computation process is based on an ability to manipulate the state of a bit or qubit. In quantum computing, a logical operation or *quantum gate* is represented by a unitary operator that transforms a quantum state in a certain way. These quantum gates have to be 2×2 unitary matrices in order to preserve the norm of Eq. 6. For example, the bit-flip or NOT operation is described by the Pauli matrix σ_x , and phase-flip operation is given by Pauli matrix σ_z . The Pauli operator, σ_x , σ_y and σ_z are unitary traceless 2-dimensional matrices which play a great role in

quantum information. They have explicit forms of

$$\sigma_x \equiv \begin{pmatrix} 0 & 1 \\ 1 & 0 \end{pmatrix}; \quad \sigma_y \equiv \begin{pmatrix} 0 & -i \\ i & 0 \end{pmatrix}; \quad \sigma_z \equiv \begin{pmatrix} 1 & 0 \\ 0 & -1 \end{pmatrix}. \quad (8)$$

One can verify that σ_x performs a bit flip by multiplying corresponding matrix and a quantum state in vector representation. This way, we can confirm that $\sigma_x|0\rangle = |1\rangle$ and $\sigma_x|1\rangle = |0\rangle$, while the bit-flip, σ_z , flips the relative phase between two basis states, $\sigma_z(c_0|0\rangle + c_1|1\rangle) = c_0|0\rangle - c_1|1\rangle$.

Examples of other important single-qubit gates include the Hadamard gate (H) and phase-shift (P_ϕ) gates:

$$H = \frac{1}{\sqrt{2}} \begin{pmatrix} 1 & 1 \\ 1 & -1 \end{pmatrix}; \quad P_\phi = \begin{pmatrix} 1 & 0 \\ 0 & e^{i\phi} \end{pmatrix}. \quad (9)$$

The importance of these gates follows from the fact that combination of H and P_ϕ can produce a transition between any two arbitrary qubit states. For example, a general qubit state up to a global phase can be achieved by the following sequence:

$$P_{\pi/2+\phi} \cdot H \cdot P_\theta \cdot H|0\rangle = \cos \frac{\theta}{2}|0\rangle + e^{i\phi} \sin \frac{\theta}{2}|1\rangle. \quad (10)$$

The possibility to generate such gates via application of external controls implies state controllability of the qubit systems, which in this special case of two-level systems is equivalent to evolution-operator controllability. Therefore, these properties of the Hadamard and phase-shift gates are equivalent to single-qubit computational universality [54].

2.1.3 Bloch-vector rotations

We have shown that control of the states of a single qubit consists of application of unitary matrices. It is useful to think of unitary matrices as the rotations of the Bloch vector described by Eq. (6). One can prove that by observing that a unitary transformation preserves the norm of a Bloch vector. At this point, in order to make a

connection with a physical realization of quantum control, it is necessary to establish the Hamiltonian description for the problem. First we consider ideal control in the absence of noise fields. For such system the time-dependent control Hamiltonian in the interaction picture with respect to the energy splitting between two levels can be generally written as

$$H(t) = \frac{1}{2}\Omega(t)\boldsymbol{\rho} \cdot \boldsymbol{\sigma} \equiv \frac{1}{2}\Omega(t)\sigma_\phi, \quad (11)$$

where $\boldsymbol{\sigma} \equiv (\sigma_x, \sigma_y, \sigma_z)$ and $\boldsymbol{\rho} \equiv (\cos \phi, \sin \phi, 0)$ is a unit vector, and $\sigma_\phi \equiv \sigma_x \cos \phi + \sigma_y \sin \phi$. It is useful to think of $\boldsymbol{\rho} \cdot \boldsymbol{\sigma}$ as the rotation generator for the Bloch vector with the rotation rate $\Omega(t)$. Then the phase parameter ϕ determines the axis in xy -plane along which the rotation occurs. If we physically realize a control field for qubit manipulation described by Eq. (11) with Hamiltonian acting for time τ , the resulting propagator can be obtained from operator equation Eq. (4):

$$U(\tau) = \exp \left(-\frac{i\sigma_\phi}{2} \int_0^\tau \Omega(t) dt \right). \quad (12)$$

The profile of control parameter $\Omega(t)$, often called Rabi frequency, is typically determined by the strength of external control field (e.g. power of the laser interacting with two-level system). In terms of qubit rotations, this parameters characterizes how fast we can perform rotations of the Bloch vector for given system and apparatus. In order to demonstrate this, we can fix a Rabi frequency to some constant value, $\Omega(t) \equiv \Omega$, then the propagator of Eq. (12) takes form

$$U(\tau) = \exp \left(-\frac{i}{2}\Omega\tau\sigma_\phi \right) = \exp \left(-\frac{i}{2}\theta\sigma_\phi \right). \quad (13)$$

Therefore, acting on the qubit state it generates a Bloch vector rotation by angle $\theta = \Omega\tau$ through the axis determined by phase ϕ . In the figure 2 we provide examples of such rotations.

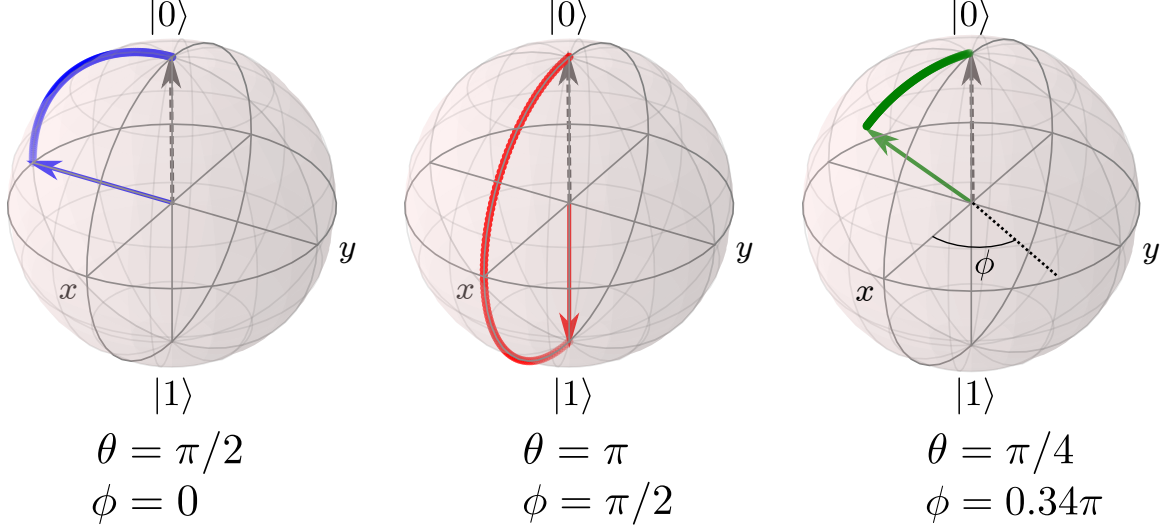


Figure 2: Examples of Bloch vector rotations generated by propagator of Eq. (13). In the case of constant Rabi frequency, rotation angle, θ , is defined through $\theta = \Omega\tau$. Rotation axis is determined by phase ϕ . In all three examples, the initial state is $|0\rangle$ (gray dashed vector).

2.1.4 Imperfections in control

In the picture considered above, ideally, we are required to have control only over two parameters, $\Omega(t)$ and ϕ , in order to produce any arbitrary rotations, and therefore, to drive an initial qubit state to any final state. However, in the real world, there are at least two main obstacles to this ideal control picture: the system typically interacts with environment and control parameters are often subject to random noise processes [54]. These two noise sources lead to an overall qubit evolution which is not unitary. These processes are related to an increase in the entropy of the qubit, transforming pure states to mixed states with randomly decaying relative phases and to energy transfer in the form of heating and dissipation.

In quantum computing, one of the key roles of quantum control is to suppress decoherence and noise in control parameters, and to achieve an evolution which approximates the target unitary process to a high fidelity. Fidelity is one of the metrics to measure the performance of quantum operations. It characterizes the probability of expected measurement outcome that follows from ideal unitary controls. It is

possible to realize quantum algorithms only if fidelities of universal gates are above the certain thresholds which are defined by the limits of fault-tolerant quantum error correction [54].

Various noise sources can be either additive or multiplicative in their nature. The strength of additive noise does not depend on the magnitude of control parameters, while multiplicative noise can grow proportionally to the value of applied control fields. In the following subsection, we discuss the common noise models for single-qubit gates in general terms.

2.1.4.1 Amplitude noise

When we realize qubit control implemented in a particular physical architecture, a controlled quantum system suffer from systematic errors introduced by the application of an imperfect control profile [1]. This type of error is called an *amplitude error*, and it effectively leads to error rotation by angle, θ' , related to desired rotation angle θ : $\theta' = \theta(1 + \epsilon)$, where ϵ is an unknown systematic error. In terms of Hamiltonian, this error originates from multiplicative error in control frequency (here and in the following subsections we consider a static Rabi frequency, Ω):

$$H_a = \frac{1}{2}\Omega(1 + \epsilon)\sigma_\phi, \quad (14)$$

which produces the propagator

$$U_a(\tau) = \exp\left(-\frac{i}{2}\theta(1 + \epsilon)\sigma_\phi\right). \quad (15)$$

Therefore, an amplitude error leads to inaccurate Bloch vector rotations and to noisy single-qubit gates.

2.1.4.2 Detuning noise

Often, there is also another type of systematic error present in the system, it may originate from random shifts in laser frequency applied to control a qubit [1]. This

error is called *detuning error* and it effects in additional small rotation through the z -axis of a Bloch sphere:

$$H_d = \frac{\Omega}{2}[\sigma_\phi + \delta\sigma_z],$$

$$U(\tau) = \exp\left(-\frac{i}{2}\theta[\sigma_\phi + \delta\sigma_z]\right). \quad (16)$$

Geometrically, the detuning error shifts the intended rotation axis out of the xy -plane.

2.1.4.3 Simultaneous noise

In the general case, we have both amplitude and detuning error present in the system, which results in inaccurate rotation angle and shifted rotation axis simultaneously [1, 2]. We refer to this situation as to *simultaneous noise*. In the case of static ϵ and δ , the Hamiltonian and propagator can be written as

$$H_s(t) = \frac{\Omega(t)}{2}[(1 + \epsilon)\sigma_\phi + \delta\sigma_z],$$

$$U(\tau) = \exp\left(-\frac{i}{2}\theta[(1 + \epsilon)\sigma_\phi + \delta\sigma_z]\right). \quad (17)$$

Graphically, all three types of noise is given in the figure 3, where we demonstrate an ideal rotation along y -axis by angle $\theta = \pi/2$ and imperfect rotations affected by systematic static noise. Constant error values, ϵ and δ , exaggerated to the large magnitude for the sake of clear demonstration.

2.1.5 Time-dependent noise

So far in the considered noise models we have been assuming unknown, static errors effectively leading to an offset constant in time. In reality, the errors in quantum system control will vary in time. In this case, we need to generalize the static DC-errors to the time-dependent noise fluctuations. Typically, an assumption of *Gaussian* (stationary) noise is accurate enough for description of the broad class of physical processes in quantum control. The spectral power of Gaussian stationary noise, $S(\omega)$,

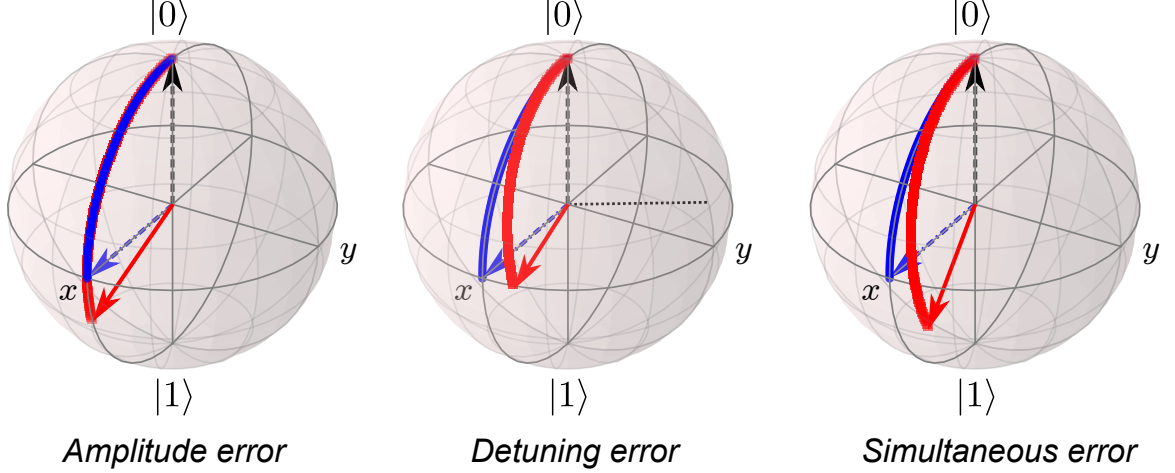


Figure 3: Graphical demonstration of amplitude (Eq. (15)), detuning (Eq. (18)) and simultaneous (Eq. (17)) error in the case of intended y -rotation by angle $\theta = \pi/2$. Ideal evolution is represented by a blue color with final state denoted by a blue dashed-dot vector along x -axis. Imperfect rotation is denoted by red color. In all three cases the chosen initial state is $|0\rangle$ (denoted by gray dashed vector). The error parameters are chosen to be large ($\epsilon = \delta = 0.2$) to clearly demonstrate the effect of noise.

and its autocorrelation function, $R(t)$, are related through Fourier transformation according to Wiener-Khinchin theorem [55]:

$$S(\omega) \equiv \int_{-\infty}^{\infty} dt e^{-i\omega t} R(t).$$

In the following chapters we will use this relation for analytical derivations and numeric noise simulations.

Formally, in order to introduce an amplitude and detuning time-dependent noise in the Hamiltonian level, the effective static errors can be replaced by their time-dependent counterparts, $\epsilon \cdot \Omega \rightarrow \beta_a(t)$ and $\delta \cdot \Omega \rightarrow \beta_d(t)$. Here, $\beta_a(t)$ and $\beta_d(t)$ represent *zero-mean* Gaussian stochastic processes with particular spectral characteristics. It is important to note that in general we assume a multiplicative nature of the amplitude noise, however in the case of fixed Rabi frequency, Ω , this noise fluctuations can be treated as the additive terms. The physical assumption of additive error model for detuning noise is quite natural. Finally, we can write down the control Hamiltonians

as

$$\begin{aligned} H_a(t) &= \frac{1}{2}[\Omega + \beta_a(t)]\sigma_\phi, \\ H_d(t) &= \frac{1}{2}[\Omega\sigma_\phi + \beta_d(t)\sigma_z]. \end{aligned} \tag{18}$$

The effect of stochastic noise on a single-qubit rotation is similar to the case of static model with an exception that in the former case the error strength changes its value through out the qubit state evolution.

2.2 Theoretical framework for time-dependent noise

2.2.1 Time-dependent error model for control protocols

In the previous sections we have discussed the idea of a single-qubit operation. As it was pointed out, any environmental and/or control errors cause the actual effect of a control protocol to differ from the intended one. In this thesis work we shall be interested here in error models that may be pictured in terms of coupling to *classical* degrees of freedom, as arising from noisy control actions and/or a fluctuating background environment – in which case the net result is the implementation of a different operation on the target system, say, $M(\theta, \phi) \neq R(\theta, \phi)$.

In the following sections, we will overview the idea of quantum control protocols which consist of multiple elementary control operations, which are sequentially implemented in such a way that the desired target operation (quantum gate) is realized while simultaneously reducing the net sensitivity to error. The mathematical frameworks and error-model assumptions employed in arriving at these constructions vary considerably, leading to different control modalities. While we refer to the relevant literature for a more complete discussion [1, 3, 56, 44, 35], we focus here on the task of effecting a target rotation on a single qubit. One class of such control protocols is a construction of composite pulses (CP) specific implementations of which will be discussed in the following chapter.

The standard error model assumed in CP constructions involves a combination of *static* (DC) pulse-length and off-resonance control errors, which we may represent as

$$M(\theta, \phi) = \exp[-i\theta\{(1 + \epsilon_a)\boldsymbol{\rho}(\phi) \cdot \boldsymbol{\sigma} + \epsilon_d\sigma_z\}/2],$$

where ϵ_a and ϵ_d quantify the amplitude and detuning offsets, respectively. CPs rely on the application of constant-amplitude control fields segmented into rotations of different durations about different axes (phase modulation) to counter these errors which, until recently [22, 20, 21, 2], have been addressed separately. If $M_a(\theta, \phi)$ (respectively, $M_d(\theta, \phi)$) denote the propagator for the special case in which *only* ϵ_a (respectively, ϵ_d) is significant, an m -th order CP protocol $M_\mu^{[m]}(\theta, \phi)$ is a sequence of elementary operations $\{M_\mu(\theta, \phi)\}$ for which [1]

$$M_\mu^{[m]}(\theta, \phi) = R(\theta, \phi) + \mathcal{O}(\epsilon_\mu^{m+1}), \quad \mu \in \{a, d\}.$$

In order to both introduce and analyze the effect of *time-dependent* amplitude and detuning errors in CP sequences, and compare them to other control protocols in a unified setting, it is necessary to formulate the control problem at the Hamiltonian (rather than propagator) level.

Let us consider a piecewise-constant chain of n discrete time-segments, each indexed by l and spanning time $t \in [t_{l-1}, t_l]$ such that, in units $\hbar \equiv 1$ and in a suitable frame, we may write a total Hamiltonian of the form

$$\begin{aligned} H(t) &= \sum_{l=1}^n G^{(l)}(t) \frac{[\Omega_l + \beta_a(t)]}{2} \boldsymbol{\rho}_a^{(l)} \cdot \boldsymbol{\sigma} + \frac{\beta_d(t)}{2} \sigma_z \\ &\equiv H_0(t) + H_{\text{err}}(t). \end{aligned} \tag{19}$$

Here, we have introduced a modulation function $G^{(l)}(t) \equiv \Theta[t - t_{l-1}]\Theta[t_l - t]$, which has unit value for $t \in [t_{l-1}, t_l]$, and is equal to zero otherwise, in order to capture the fact that the control is implemented in a piecewise-constant fashion. The ideal control field amplitude for the l -th segment is denoted by Ω_l , and its axis of rotation by $\boldsymbol{\rho}_a^{(l)} \equiv \boldsymbol{\rho}(\phi_l) = (\cos \phi_l, \sin \phi_l, 0)$. The two *zero-mean Gaussian* (stationary) stochastic

processes $\beta_a(t)$ and $\beta_d(t)$ model amplitude and detuning noise, respectively. We assume that both such processes enter the dynamics additively, and are independent of the ideal amplitude and phase of the control, while also being *mutually independent*, that is, $\langle \beta_a(t)\beta_d(t') \rangle = 0$.

The total Hamiltonian in Eq. (19) may be separated into ideal plus error Hamiltonians by isolating the noise terms proportional to β_μ . That is, acting alone, $H_0(t)$ generates the unitary propagator $U_0(t, 0) = \sum_{l=1}^n G^{(l)}(t)U_0(t, t_{l-1})R'_{l-1}$, which describes a sequence of n consecutive elementary control operations $R_l \equiv R(\theta_l, \phi_l)$, $l = 1, \dots, n$, executed over a total gating time $\tau \equiv t_n$. Here, the operator $U_0(t, t_{l-1}) \equiv \exp[-i\Omega_l(t - t_{l-1})\boldsymbol{\rho}_a^{(l)} \cdot \boldsymbol{\sigma}/2]$ is the time-dependent propagator for the l -th elementary pulse, such that $\theta_l = \Omega_l(t_l - t_{l-1})$ and $U_0(t_l, t_{l-1}) = R_l$. At the end of the sequence, $U_0(\tau, 0) = R(\theta, \phi) = R'_n$ (the desired target operation), where $R'_l \equiv R_l R_{l-1} \dots R_0$ and $R_0 \equiv I$.

Following [3], the total evolution operator $U(t, 0)$, generated by the controlled Hamiltonian in Eq. (19) may then be written as $U(\tau, 0) \equiv U_0(\tau, 0) \exp[-i\Phi(\tau)]$, where the “error action operator” encapsulates the effect of $H_{\text{err}}(t)$ and, to the lowest order in a perturbative Magnus-series expansion, we may write

$$\Phi(\tau) \approx \Phi_1(\tau) = \int_0^\tau dt U_0^\dagger(t, 0) H_{\text{err}}(t) U_0(t, 0). \quad (20)$$

Calculating this quantity requires consideration of all (ideal) time-ordered control operations enacted during the sequence; accordingly, let us define “control vectors” as follows [4]:

$$\begin{aligned} \boldsymbol{\rho}_a(t) &\equiv \frac{1}{2} \sum_{l=1}^n G^{(l)}(t) \boldsymbol{\rho}_a^{(l)} \boldsymbol{\Lambda}^{(l-1)}, \\ \boldsymbol{\rho}_d(t) &\equiv \frac{1}{2} \sum_{l=1}^n G^{(l)}(t) \boldsymbol{\rho}_d^{(l)}(t - t_{l-1}) \boldsymbol{\Lambda}^{(l-1)}, \end{aligned}$$

where the matrices (vectors) $\boldsymbol{\Lambda}^{(l-1)}$ ($\boldsymbol{\rho}_d^{(l)}(t - t_{l-1})$) have components

$$\begin{aligned}\Lambda_{ij}^{(l-1)} &= \text{Tr}[R_{l-1}^\dagger \sigma_i R_{l-1}' \sigma_j]/2, \\ \rho_{d,j}^{(l)}(t - t_{l-1}) &= \text{Tr}[U_0^\dagger(t, t_{l-1}) \sigma_z U_0(t, t_{l-1}) \sigma_j]/2,\end{aligned}$$

for $i, j \in \{x, y, z\}$. Thus, $\Phi_1(\tau) = \mathbf{a}(\tau) \cdot \boldsymbol{\sigma}$, where the “error vector”,

$$\mathbf{a}(\tau) \equiv \int_0^\tau dt [\beta_a(t) \boldsymbol{\rho}_a(t) + \beta_d(t) \boldsymbol{\rho}_d(t)],$$

captures the difference between the actual and target control operations, for each realization of the noise.

2.2.2 Performance measure and filter-transfer functions

In order to gain useful information about the overall performance of a CP protocol, we must characterize performance across an ensemble of noise realizations. As a figure of merit, we consider the ensemble-averaged (denoted by $\langle \cdot \rangle$) propagator fidelity, which in our qubit setting reads

$$\mathcal{F} = \frac{1}{4} \left\langle |\text{Tr}[U_0^\dagger(\tau, 0) U(\tau, 0)]|^2 \right\rangle. \quad (21)$$

In contrast to the worst-case fidelity, the average fidelity takes into account different noise realizations and refers to their average outcome.

In the (weak-noise or/and short-time) limit where the first-order description of Eq. (20) is accurate, we may further write [4, 50]:

$$\mathcal{F} \approx 1 - \langle a(\tau)^2 \rangle, \quad a(\tau) \equiv [\mathbf{a}(\tau) \cdot \mathbf{a}(\tau)]^{1/2}.$$

This quantity is most conveniently calculated in the Fourier domain; introducing the noise power spectral densities,

$$S_\mu(\omega) \equiv \int_{-\infty}^{\infty} dt e^{-i\omega t} \langle \beta_\mu(t_0) \beta_\mu(t_0 + t) \rangle$$

for $\mu \in \{a, d\}$, and exploiting the stationarity and independence properties of the noise sources, we finally obtain the following expression for the (first-order) fidelity loss:

$$1 - \mathcal{F} \approx \frac{1}{2\pi} \int_{-\infty}^{\infty} \frac{d\omega}{\omega^2} \sum_{\mu=a,d} S_{\mu}(\omega) F_{\mu}(\omega). \quad (22)$$

Here, $F_{\mu}(\omega) \equiv \boldsymbol{\rho}_{\mu}^*(\omega) \cdot \boldsymbol{\rho}_{\mu}(\omega)$ is the *generalized FF* for amplitude ($\mu = a$) and detuning ($\mu = d$) respectively, defined in terms of the frequency-domain control vectors, $\boldsymbol{\rho}_{\mu}(\omega) = -i\omega \int_0^{\tau} dt \boldsymbol{\rho}_{\mu}(t) e^{i\omega t}$.

When we consider the realistic noise spectra, we take into account the frequency cut-offs, ω_{\min} and ω_{\max} , and we integrate over positive frequencies only (it yields the factor of 2 in front of the integral):

$$1 - \mathcal{F} \approx \frac{1}{\pi} \int_{\omega_{\min}}^{\omega_{\max}} \frac{d\omega}{\omega^2} \sum_{\mu=a,d} S_{\mu}(\omega) F_{\mu}(\omega). \quad (23)$$

The FFs characterize the spectral properties of the applied control and thus provide a simple quantitative means to compare the control protocols of interest (see Table 1) in the presence of time-dependent Gaussian noise [46, 4]. In Fig. 4 we demonstrate an example of FF for primitive gate and example of spectral power. In order to estimate the gate performance for frequency window determined by ω_{\min} and ω_{\max} , we are interested in overlap of two functions (Fig. 4) within that particular frequency range denoted by shaded area. In general, one may interpret these functions by considering the transfer function of a high-pass filter, including passband, stopband, and roll-off. The filter roll-off, captured by the slope of the FF near zero frequency, serves as a lower bound on the order of error suppression in the presence of time-dependent noise [57]. This approach has been validated for nontrivial control - including CP constructions - in recent experiments [50]. On the theoretical side there have been a recent development of general filter-transfer function approach to quantum control problems [58]. We next proceed to calculate and present independently the FFs for both amplitude and detuning quadratures.

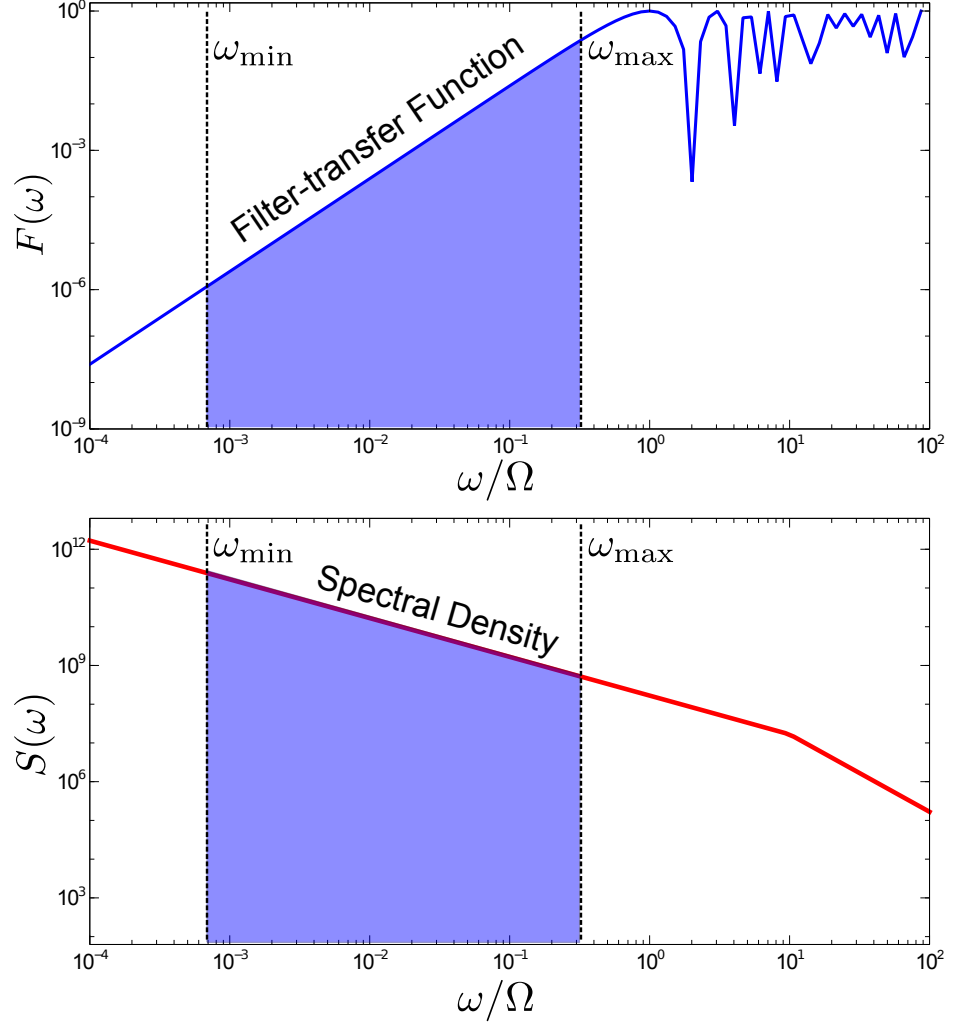


Figure 4: Example of filter-transfer function (top) and spectral density (bottom) that can be used for estimating performance of a control operation. Fidelity loss is estimated according to Eq. (23) as an overlap integral of these two functions in a frequency domain within particular limits (in this example it is denoted by a shaded area).

We can notice that in optimal control settings, analytical integral in Eq. (68) may serve a role of objective function that should be minimized in order to achieve a better performance. General approach of optimal control will be discussed in the next section.

2.3 Optimal control

Optimal control theory is widely used in quantum control systems for implementation of quantum logical operations or quantum gates. It is also a method to reduce the effects of the noise fields in the best possible way, with respect to some measure of performance [59, 52]. Basically, the process of finding an optimal control solution is a search over a landscape corresponding to an objective function as a function of possible control parameters. The objective or cost function can be determined by fidelity of logical operation or any other measure for performance of suppressing a present noise. In this way, a main goal of optimal control is to locate extrema on the given configuration space, which is to find such values of control parameters that provide the best performance.

In recent years, applications of optimal control for mitigating noise and environment effects in quantum computation and quantum information have become very popular [59, 60, 61, 62, 63, 64, 65, 66, 67, 68, 34, 69]. Typically, the qubit states are transformed by external controls characterized by parameters such as a shape of applied pulses. These parameters are obtained by the methods of optimal control associated with various numerical optimization techniques. Applying such control protocols makes it possible to achieve an effect of error suppression to a tolerable level where quantum error correction codes are practically feasible [54]. Before we employ an optimal quantum control, we are required to attain a detailed knowledge of the quantum system and noise processes from which the system can suffer.

There are at least two distinctive types of optimal control theory applications for

quantum control. In one way, it is used to derive solutions for state-to-state transitions [70, 71]. Here, the task is to design a control Hamiltonian that would drive the given state of quantum system to a target state, taking into account constraints and limitations of physical implementations. The second type of applications is related to a synthesis of a particular desired unitary gate, that can be a logical element of a quantum algorithm. In general, the problem for both applications can be extended to allow an optimal control in the presence of noise fields caused by interaction with a quantum bath or imperfections in control apparatus.

In the following, we briefly formulate both types of optimal control. Although in this thesis, when implement an optimal control, we focus on synthesizing of desired quantum gates, as this problem plays a primary role in quantum computing.

2.3.1 Optimal control for state-to-state transitions

We discuss quantum state-to-state transitions according to work by Kosloff *et al.* [70] and Shi and Rabitz [71]. As it was mentioned above, the dynamics of an isolated quantum system under the external control fields $u(t)$ described by the time-dependent Schrödinger equation:

$$\begin{aligned} i\frac{d|\psi(t)\rangle}{dt} &= H(u(t))|\psi(t)\rangle, \\ |\psi(0)\rangle &= |\psi_0\rangle. \end{aligned} \tag{24}$$

The dependence of Hamiltonian $H(u(t))$ on control field in the interaction picture can be often written in the form $H(u(t)) = -\boldsymbol{\mu} \cdot \mathbf{u}(t)$. Here we can consider $\boldsymbol{\mu}$ as the transition dipole operator. The task of optimal control is to design such time-dependent control $u(t)$ that would steer the system from given state $|\psi_0\rangle$ to a particular target state $|\phi\rangle$ at final time $t = T$.

The physical objective for this type of problem will have a form of a functional consisting of *terminal* and *integral* components. The terminal component $\Phi_s[\langle \mathcal{O}_\phi(T) \rangle]$ is determined by the distance of the state $|\psi(T)\rangle$ from the target state $|\phi\rangle$, where

expectation value of projection operator $\mathcal{O}_\phi \equiv |\phi\rangle\langle\phi|$ is given by

$$\langle\mathcal{O}_\phi(t)\rangle = \langle\psi(t)|\mathcal{O}_\phi|\psi(t)\rangle = |\langle\phi|\psi(t)\rangle|^2. \quad (25)$$

The integral component of functional, $\mathcal{I}_s[\langle P(t)\rangle]$, characterizes the distance of the system state from its target dynamic values throughout some particular time interval specified in a control problem. If $|\xi(t)\rangle$ is a particular target trajectory for the quantum system, then $P(t)$ can be a projection operator to that state: $\mathcal{O}_\xi \equiv |\xi(t)\rangle\langle\xi(t)|$. If we focus only on integral functional, this optimal control problem sometimes is called a *local* control. The approach would be called *global* if we consider only a terminal functional, i.e. we require a target state to match only at time $t = T$.

Typically, there is also a third term in a complete objective functional that characterizes a measure of the energy applied to the system due to control field interactions. We define that functional that sets the fluence penalty on the applied control as

$$\mathcal{L}[u(t)] = \int_0^T \alpha(t)u^2(t)dt; \quad \alpha(t) \geq 0, \quad (26)$$

where $\alpha(t)$ is a weighting parameter.

The total objective functional would consist of three described terms:

$$\mathcal{J}_s[u(t), \psi(t)] = \Phi_s[\langle\mathcal{O}_\phi(T)\rangle] + \mathcal{I}_s[\langle P(t)\rangle] + \mathcal{L}[c(t)]. \quad (27)$$

We should now take into account a dynamic constraint which is governed by Schrödinger equation, Eq. (24) by introducing time-dependent Lagrange multiplier $|\lambda(t)\rangle$. It will contribute to the objective functional by the following term:

$$\mathcal{M}_s[u(t), \psi(t), \lambda(t)] = -2\text{Re} \left[\int_0^T \langle\lambda(t)|(\dot{\psi}(t) + iH(u(t))\psi(t))\rangle dt \right]. \quad (28)$$

If we sum up \mathcal{J}_s and \mathcal{M}_s we obtain an unconstrained objective functional $\mathcal{J}'_s = \mathcal{J}_s + \mathcal{M}_s$. Solving an optimal control problem with respect to that functional leads to the desired optimal solutions for $u(t)$.

The two following forms for functionals Φ_s and \mathcal{I}_s are commonly used:

$$\begin{aligned}\Phi_s &= |\langle \phi | \psi(T) \rangle|^2, \\ \mathcal{I}_s &= \int_0^T \omega(t) \langle \psi(t) | P(t) | \psi(t) \rangle dt.\end{aligned}\tag{29}$$

Here $\omega(t)$ is weighting factor of the integral objective and $P(t)$ is the projection operator on a dynamic trajectory of states.

The problem can be converged to the system of Euler-Lagrange equations

$$i \frac{d|\psi(t)\rangle}{dt} = H(u(t))|\psi(t)\rangle, \quad |\psi(0)\rangle = |\psi_0\rangle,\tag{30}$$

$$|\dot{\lambda}(t)\rangle = -iH(t)|\lambda(t)\rangle + \omega(t)P(t)|\psi(t)\rangle, \quad |\lambda(T)\rangle = \langle \phi | \psi(T) \rangle |\phi\rangle.\tag{31}$$

Gradient of functional \mathcal{J}'_s with respect to the control $u(t)$ us written as

$$\nabla_u \mathcal{J}'_s = -\alpha(t)u(t) + \text{Im}[\langle \lambda(t) | \nabla_u H(t) | \psi(t) \rangle].\tag{32}$$

Using the method of variation of parameters [72], the equation Eq. (31) can be solved as

$$|\psi(t)\rangle = U(t, T)|\lambda(T)\rangle - U(t, 0) \int_t^T \omega(t') U^\dagger(t', 0) P(t') |\psi(t')\rangle dt',\tag{33}$$

where $U(t_2, t_1)$ is the unitary time-evolution which corresponds to propagation of the Lagrange multiplier state from $|\lambda(t_1)\rangle$ to $|\lambda(t_2)\rangle$. In the section 2.3.3, we will briefly mention which optimization techniques can be employed for numerical solutions of this nonlinear problem.

2.3.2 Optimal control for the evolution operator

The control objective for evolution operator is to maximize the quantum gate fidelity which is equivalent to minimizing a distance between the propagator at final time $t = T$ and the target gate R . This requirement can be incorporated in the following terminal objective functional:

$$\Phi_v[U(T)] = 1 - \|V - U(T)\|,\tag{34}$$

where $\|\cdot\|$ denotes a matrix norm.

We remind that evolution of $U(t)$ follows the operator Schrödinger equation:

$$i\dot{U}(t) = H(u(t))U(t), \quad U(0) = \mathbb{1}. \quad (35)$$

Similarly to state-to-state transition problem, we add the dynamic constraint (Eq. (35)) by introducing a time-dependent Lagrange multiplier operator $B(t)$ to an objective functional as an additional term \mathcal{M}_v :

$$\mathcal{M}_v[u(t), U(t), B(t)] = -2\text{Re} \left(\int_0^T \text{Tr}\{B^\dagger(t)[\dot{U}(t) + iH(t)U(t)]\} dt \right). \quad (36)$$

The total unconstrained objective functional is then given by

$$\mathcal{J}'_v[u(t), U(t), B(t)] = \Phi_v[U(T)] + \mathcal{M}_v[u(t), U(t), B(t)] + \mathcal{L}[u(t)], \quad (37)$$

where $\mathcal{L}[u(t)]$ is the fluence penalty term defined the same way as in Eq. (26). From these expressions we can derive the following coupled Euler-Lagrange equations [72]:

$$\begin{aligned} i\dot{U}(t) &= H(u(t))U(t), \quad U(0) = \mathbb{1}, \\ i\dot{B}(t) &= H(u(t))B(t), \quad B(T) = \nabla_U \Phi_v[U(T)]. \end{aligned} \quad (38)$$

The gradient of objective functional with respect to the control field will have the form

$$\nabla_u \mathcal{J}'_v = -\alpha(t)u(t) + \text{Im}\{\text{Tr}[B^\dagger(t)\nabla_u H(t)U(t)]\}. \quad (39)$$

If Hamiltonian has the form $H(t) = -\boldsymbol{\mu}\mathbf{u}(t)$, the gradient of $\nabla_u H(t)$ with respect to control fields is $\nabla_u H(t) = -\boldsymbol{\mu}$. Therefore, we can compute gradient of objective functional Eq. (39) based on control field $u(t)$ and propagator $U(t)$ which can be calculated from Schrödinger equation. Thus, it is possible now to use gradient-based optimization algorithms that provide optimal control profiles of $u(t)$ that maximize fidelity of logical gates. In the following section we overview different optimization methods and discuss in details techniques that we use in this work.

2.3.3 Optimization methods

There is a number of optimization algorithms that have been adapted and developed for optimal control of quantum systems. They can be used to solve Euler-Lagrange equations discussed above (Eq. (30) - Eq. (32) and Eq. (38), Eq. (39)), provided that we can make a guess for initial control field. Among common optimization algorithms are the Krotov method [73, 69, 74, 75], conjugate gradient search method [70, 71], monotonically convergent algorithms [76, 77, 78, 79], and the gradient ascent pulse engineering algorithm (GRAPE) [64, 74, 80]. There is an approach based on combining different method which provides a faster convergence [81]. More comprehensive reviews on optimization algorithms can be found elsewhere [74]. Here we focus on algorithms that were used in this thesis work for the quantum systems in the presence of time-dependent noise.

2.3.3.1 GRAPE

Gradient ascent pulse engineering (GRAPE) algorithms initially have been developed for the design of pulse sequences in NMR spectroscopy [64] and later have been extended to different applications and have found a wide use in quantum control theory [74, 80]. In the following we present the theoretical basis to the algorithm.

Here we describe a quantum state by the density operator $\rho(t)$. Then its evolution in the absence of relaxation is determined by the Liouville-von Neuman equation [16] which is equivalent of Schrödinger equation for density operators:

$$\dot{\rho}(t) = -i[(H_0 + \sum_{k=1}^m u_k(t)H_k), \rho(t)]. \quad (40)$$

Here, as in previous sections, H_0 is the free evolution Hamiltonian, and H_k and $\{u_k(t)\}$ characterize available control settings. The problem is to obtain such control amplitudes $\{u_k(t)\}$ that drive an initial density matrix $\rho(0) = \rho_0$ to a density matrix $\rho(T)$, where T is a given final time. In this case, the objective functional Φ_0 is defined

as an overlap of a given target operator C and final density operator $\rho(T)$:

$$\Phi_0 = \langle C | \rho(T) \rangle = \text{Tr}[C^\dagger \rho(T)]. \quad (41)$$

We assume that the total evolution time T can be discretized in N equal steps each of duration $\delta t = T/N$ in the way that during j -th time step each control amplitude $u_k(j)$ takes a constant value. In this case we can write down the evolution propagator during a time step j as

$$U_j = \exp\{-i\Delta t[(H_0 + \sum_{k=1}^m u_k(j)H_k)]\}. \quad (42)$$

Then the final density operator and objective functional would be given by

$$\rho(T) = U_N \dots U_1 \rho_0 U_1^\dagger \dots U_N^\dagger \quad (43)$$

$$\Phi_0 = \langle C | U_N \dots U_1 \rho_0 U_1^\dagger \dots U_N^\dagger \rangle. \quad (44)$$

The objective functional can be rewritten as

$$\Phi_0 = \langle \lambda_j | \rho_j \rangle, \quad (45)$$

where λ_j is the target operator C at time $t = j\Delta t$ propagated backward:

$$\lambda_j = U_{j+1}^\dagger \dots U_N^\dagger C U_N \dots U_{j+1}, \quad (46)$$

and ρ_j is the state at the same time:

$$\rho_j = U_j \dots U_1 \rho_0 U_1^\dagger \dots U_j^\dagger. \quad (47)$$

Let us find out how the objective functional changes when we modify the control fields. The following formula will be useful here

$$\frac{d}{dx} e^{A+xB} \big|_{x=0} = e^A \int_0^1 e^{A\tau} B e^{-A\tau} d\tau. \quad (48)$$

If we perturb the control amplitudes as $u_k(j) + \delta u_k(j)$, the change in the propagator of Eq. (42) to first order in $\delta u_k(j)$ is

$$\delta U_j = -i\Delta t \delta u_k(j) \overline{H}_k U_j, \quad (49)$$

where \overline{H} is defined from

$$\overline{H}_k \Delta t = \int_0^{\Delta t} U_j(\tau) H_k U_j(-\tau) d\tau. \quad (50)$$

The propagator $U_j(\tau)$ can be determined from Eq. (42). Using Eq. (45) and Eq. (49), we can obtain to the first order in Δt (in this approximation, $\overline{H}_k \simeq H_k$)

$$\frac{\delta \Phi_0}{\delta u_k(j)} = -\langle \lambda_j | i \Delta t [H_k, \rho_j] \rangle. \quad (51)$$

We can notice that if we update the control fields according to the scheme

$$u_k(j) \rightarrow u_k(j) + \epsilon \frac{\delta \Phi_0}{\delta u_k(j)}, \quad (52)$$

where ϵ is a sufficiently small step size. This is the core part of the GRAPE algorithm with a basic flowchart given in Fig. 5.

2.3.3.2 Simulated annealing

So far we have been considering the gradient-based optimization methods. One of the common obstacles of these methods is that they can lead to solutions which are local rather than global extrema. Finding a global maximum or minimum is especially hard problem when we deal with multi-dimensional control landscape.

Here we discuss a heuristic technique called simulated annealing (SA) which can be often used to locate a good approximation to the global extremum. This method was independently developed by Scott Kirkpatrick et al. [82] and by Vlado Černý [83]. Inspired by thermodynamics, it is an adaptation of the Metropolis-Hastings algorithm, a Monte Carlo method to generate sample states of a thermodynamic system [84].

SA have been successfully used for a number of practical applications including the traveling salesman problem [85] and designing complex integrated circuits [82, 86]. Despite the fact that SA is often used for discrete combinatorial minimization problems it is also widely used for problems with continuously variable parameters. Therefore, the technique can be employed in quantum control applications as well.

Basic Routine of GRAPE algorithm

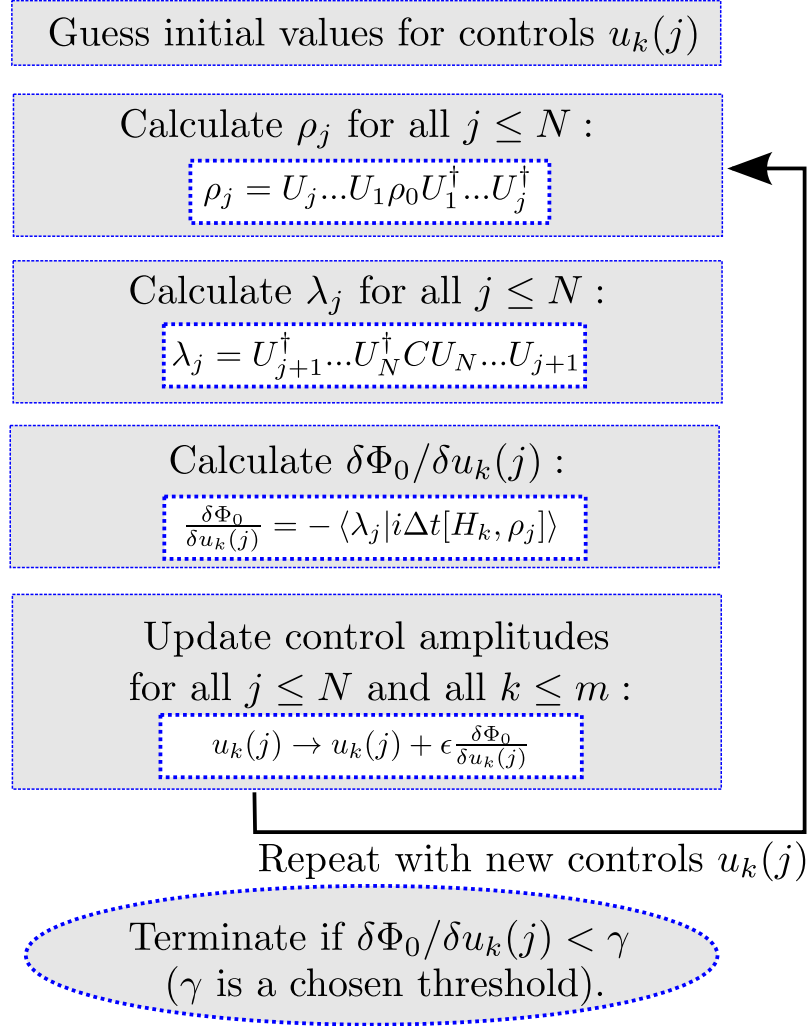


Figure 5: Basic flow for gradient ascent pulse engineering (GRAPE) algorithm. See text for details.

At the heart of the heuristic approach of SA is an analogy with cooling and crystallization of a material. When the temperature is lowered the atoms are often able to form an ordered structure that corresponds to the state of minimum energy. The key notion is the process of slow cooling which allows atoms to redistribute as they lose their mobility. In thermodynamics, the system in thermal equilibrium at temperature T has its energy probabilistically distributed among different energy states E according to Boltzmann distribution:

$$P(E) \sim \exp\left(-\frac{E}{kT}\right). \quad (53)$$

Therefore, even at low temperature, there is a non-zero probability that a system can transfer to a high energy state, and there is a chance for the system to get out of a local energy minimum which can potentially help find a global minimum. In the contrast to gradient-based methods, the SA allows us to explore the control space more extensively as the system can sometimes go uphill and sometimes downhill. But when the temperature gets lower the probability of any significant uphill excursion becomes lower (Eq. (53)). In this way, if we design an optimization routine which goes over control landscape similarly to the way how thermodynamic system are cooled down we can achieve an accurate approximation to global minimum. The basic steps of SA algorithm are given in Fig. 6.

2.3.3.3 *Walsh modulation*

During the search for optimized control protocols we have to explore the control space of modulated parameters, such as Rabi frequency or rotation phase. Employing a basis set of discrete functions for control modulation can greatly reduce the dimensionality of the search space. One such basis consists of *Walsh functions*, which are represented by trains of square pulses with the allowed binary states being -1 and +1. Forming an orthonormal-complete family defined in a piecewise-constant manner, Walsh functions can be used for practical implementation of control profiles

Basic Steps of Simulated Annealing algorithm

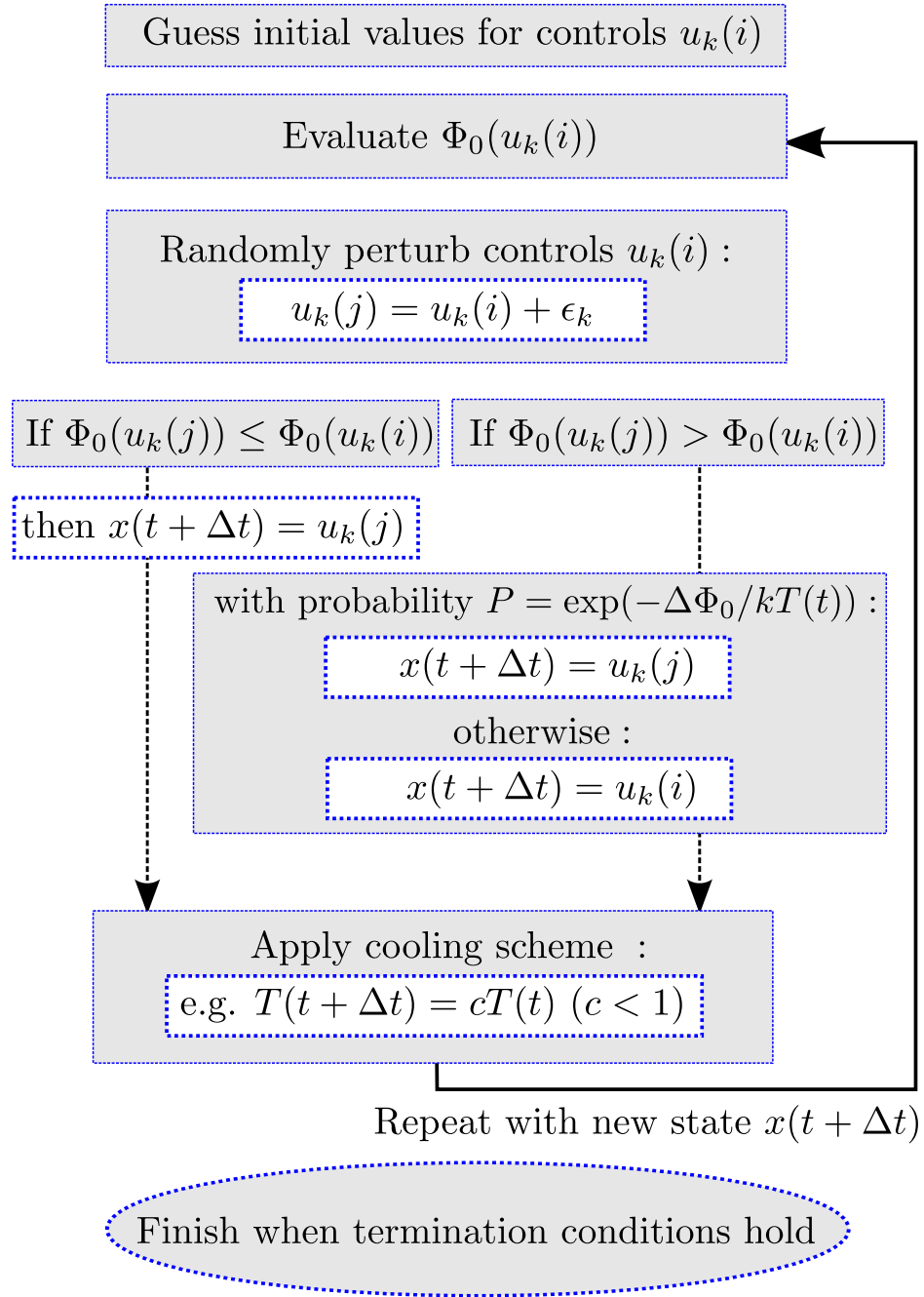


Figure 6: Basic flow for Simulated Annealing algorithm. In accordance with thermodynamical analogy, x plays a role of a system state (described by set of controls $u_k(j)$); objective function Φ_0 is an effective energy of system that we need to minimize; $T(t)$ is an effective temperature at time t ; $\Delta\Phi_0 = \Phi_0(u_k(j)) - \Phi_0(u_k(i))$. Termination conditions are typically based on a low temperature threshold or certain number of repetitions.

with discrete clocking [87]. For decades Walsh functions have been used in many applications of digital electronics, and recently they have been found to be a powerful resource for quantum information [88, 89]. They also have been used in quantum control settings for noise-filtering [90, 50].

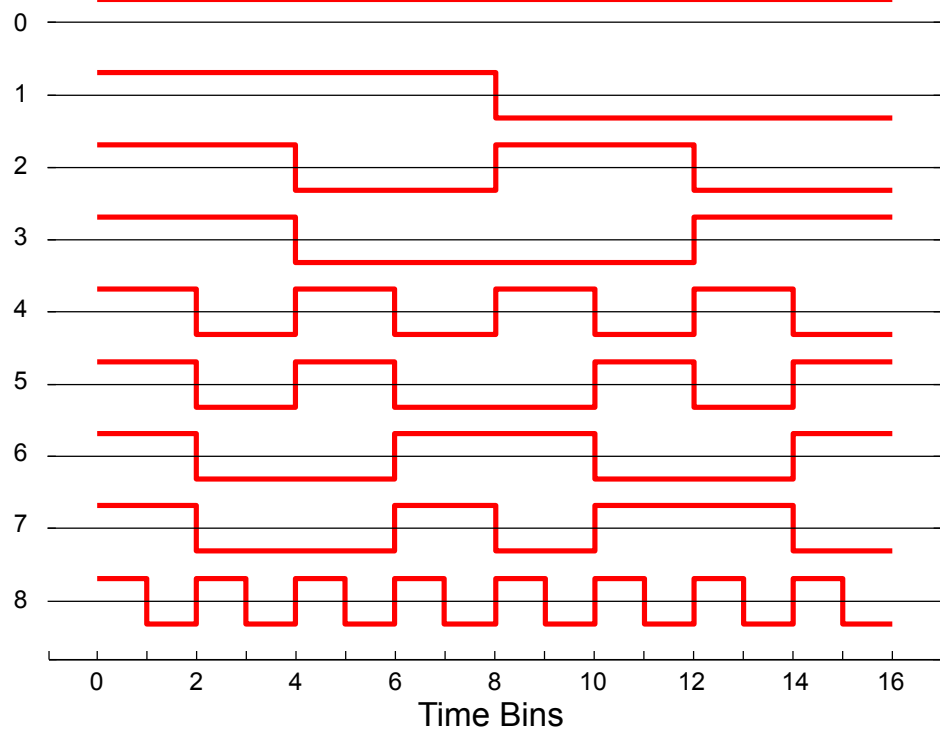


Figure 7: First 8 Walsh functions in Paley ordering

In this work we will use a *Paley* or *dyadic ordering* of Walsh functions, where the function of order k is defined as

$$\text{PAL}_k(x) = \prod_{j=1}^m R_j(x)^{b_j}, \quad (54)$$

$$R_j(x) := \text{sgn}[\sin(2^j \pi x)], \quad x \in [0, 1], \quad j \geq 0, \quad (55)$$

where $R_j(x)^{b_j}$ is the j th Rademacher function [91], which is a periodic square wave with 2^{j-1} times of zero crossings in one cycle. The superscript b_j is defined from the binary representation of order k . The first eight Walsh functions in Paley order are given in Fig. 7.

Having defined the Walsh basis, we can now represent a time-dependent piecewise-constant function through the expansion with coefficients C_k . For example, if the total duration of a control sequence is τ , the Rabi frequency $\Omega(t)$ can be expanded as

$$\Omega(t) = \sum_{k=0}^N C_k \text{PAL}_k(t/\tau). \quad (56)$$

In optimization routine, with this expansion we can modify a set of coefficients C_k instead of perturbing the control fields. This often leads to a faster convergence due to reduced dimensionality of control landscape [90, 50].

2.4 *Conclusion*

This chapter discussed some aspects of general formalism for quantum control theory. We have demonstrated the importance of single-qubit rotations for quantum computation. Imperfections in control fields and interaction between a quantum system and environment in general prevent an accurate manipulation of the states of system. Robust qubit control with errors below some threshold is one of the main requirements for fault-tolerant quantum computations, therefore quantum control protocols should be applied which reduce the effect of noise. We discussed how the performance of arbitrary control protocols consisting of qubit rotations can be considered in a unified theoretical framework. One of the approaches to design such control protocols can be adopted from optimal control theory. In the following chapter we consider how robust specific implementations of quantum control protocols to time-dependent noise.

CHAPTER III

COMPOSITE PULSE SEQUENCES IN THE PRESENCE OF TIME-DEPENDENT NOISE

Chingiz Kabytayev, Todd J. Green, Kaveh Khodjasteh, Michael J. Biercuk, Lorenza Viola, and Kenneth R. Brown “Robustness of composite pulses to time-dependent control noise”. *Phys. Rev. A* **90**, 012316 (2014).

In this chapter we use a combination of analytic formulations based on FFs and numerical simulations to demonstrate that CPs are able to effectively suppress control errors caused by time-dependent processes possessing realistic noise power spectra. Specifically, we consider a variety of both standard and concatenated CP sequences on a single qubit, as well as simple DCG protocols, and compare their performance within a unified control framework. Remarkably, robust performance of CP sequences is found *up to fluctuations as fast as $\sim 10\%$ of the Rabi frequency*, providing an explicit *quantitative* characterization of the sensitivity of these approaches to time-dependent control noise. Calculations show that even under such noise environments, which are beyond the static ones originally assumed for CPs, predicted fidelities are at least comparable to DCGs in scenarios where protocols of both kind are applicable. We present a geometric interpretation of CP performance under time-dependent amplitude noise in order to provide insight into this behavior, further linking the FF formalism with known techniques in CP construction [1].

3.1 *Composite Pulses*

The representative CP sequences we consider are given in Table 1. For instance, SK1 and BB1 are first- and second-order CPs correcting for pure amplitude errors [19, 18], whereas CORPSE is a first-order compensating sequence for pure detuning errors [18, 92]. Simultaneous errors can be systematically suppressed for arbitrary (θ, ϕ) by applying concatenated CPs [2], such as reduced CinSK (CORPSE in SK1) and reduced CinBB (CORPSE in BB1).

DCG protocols are constructed from general Hamiltonian models for finite-dimensional open quantum systems exposed to non-Markovian decoherence due to quantum or, as considered here, classical environments. This is to be contrasted with CP constructions which are obtained without making reference to an underlying physical model for the intervening error dynamics. In the simplest case DCGs employ piecewise-constant amplitude and phase modulation of the applied control fields across a sequence of carefully designed elementary segments. Through this approach, the error-sensitivity of the target operation is perturbatively minimized to a given order [3]. More general analytical DCG constructions are also possible, involving “stretching and scaling” arbitrary control profiles. In the present setting, we take advantage of formal similarity of the propagator $M(\theta, \phi)$ under pure off-resonance errors ($\epsilon_a = 0$) to the one arising from single-axis classical decoherence in the DCG context. Specifically, the representative DCG we study is a first-order three-segment sequence, obtained from general constructions in the special case $\theta = \pi$ [3, 4] (see also Table 1).

3.2 *Robustness of composite pulses to time-dependent noise*

3.2.1 *Analytical results*

We begin by analyzing the effect of a single noise source, as described by the appropriate generalized FF introduced in the previous chapter. Results are summarized

Table 1: CP sequences correcting the target rotation $R(\theta, 0)$ against different error models [1, 2]. Here, $\phi_1 = \cos^{-1}(-\theta/4\pi)$, $k = \arcsin[\sin(\theta/2)/2]$, $\alpha = 2\pi + \theta/2$, a : amplitude noise; d : detuning noise; s : simultaneous amplitude and detuning noise [see text]. For the DCG sequence [3, 4], $\Omega_1 = \Omega$, $0 \leq t < t_1 \equiv \tau/4$; $\Omega_2 = \Omega/2$, $t_1 \leq t < t_2 \equiv 3\tau/4$; $\Omega_3 = \Omega$, $t_2 \leq t < t_3 \equiv \tau$.

CP / Error model	(θ_1, ϕ_1)	(θ_2, ϕ_2)	(θ_3, ϕ_3)	(θ_4, ϕ_4)	(θ_5, ϕ_5)	(θ_6, ϕ_6)
SK1 / a	$(\theta, 0)$	$(2\pi, -\phi_1)$	$(2\pi, \phi_1)$	-	-	-
BB1 / a	$(\theta, 0)$	(π, ϕ_1)	$(2\pi, 3\phi_1)$	(π, ϕ_1)	-	-
CORPSE / d	$(\alpha - k, 0)$	$(2\pi - 2k, \pi)$	$(\theta/2 - k, 0)$	-	-	-
Reduced CinSK / s	$(\alpha - k, 0)$	$(2\pi - 2k, \pi)$	$(\theta/2 - k, 0)$	$(2\pi, -\phi_1)$	$(2\pi, \phi_1)$	-
Reduced CinBB / s	$(\alpha - k, 0)$	$(2\pi - 2k, \pi)$	$(\theta/2 - k, 0)$	(π, ϕ_1)	$(2\pi, 3\phi_1)$	(π, ϕ_1)

in the two top panels of Fig. 9, where we also show, for comparison, FFs for an uncorrected (elementary or “primitive”) π -rotation. As the latter is expected to have no error-suppressing properties, a comparison of the FFs for CP protocols against the primitive rotation reveals their relative performance advantages; a steeper slope indicates improved (higher-order) error suppression. We compute fidelity loss as a function of spectral parameter, ω_b , that characterizes the knee of the roll-off from $1/f$ to $1/f^2$ behavior. In Fig. 8 we show three examples of such spectrum with different values of ω_b .

As we observe from Fig. 9, all compensating sequences show the expected first-order suppression of errors against which they are designed to be effective, in the low-frequency limit. At the same time, they show no improvement over the primitive for the uncompensated error quadrature. Remarkably, our analysis reveals that the crossover frequency at which the FF for CP protocols becomes larger than that for the primitive is as high as $\sim 10\%$ of the driving frequency Ω . Accordingly, in circumstances where the noise power spectral density is dominated by frequencies below this value, CP sequences are still expected to provide robust error-suppressing performance.

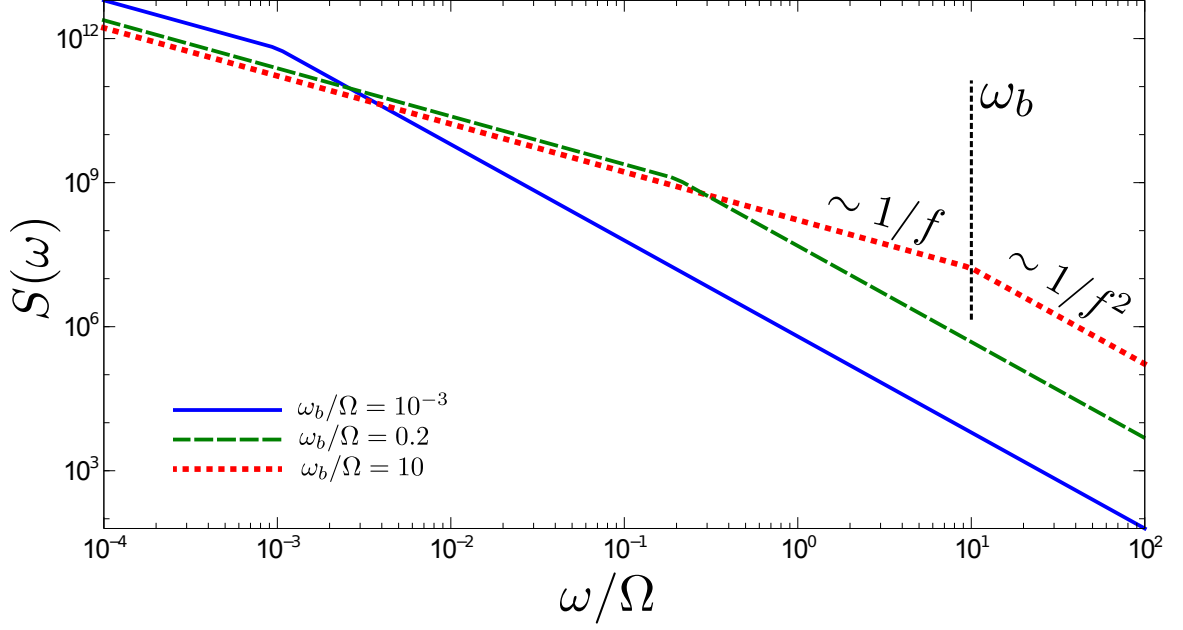


Figure 8: Example of various shapes for spectral density for three different values of a roll-off knee, ω_b .

3.2.2 Geometric picture

For amplitude noise, it is possible to make connections between the form of the amplitude FF and geometric models commonly used to describe CPs [1, 21, 93, 23]. One may represent a compensating sequence as an initial target rotation followed by correction rotations, captured through a set of vectors in a multi-dimensional space. Direct calculation shows that a sequence correcting DC errors to the first order satisfies the condition:

$$\sum_l \Omega(t_l - t_{l-1}) \tilde{\rho}_a^{(l)} = 0, \quad \tilde{\rho}_a^{(l)} \equiv \rho_a^{(l)} \mathbf{\Lambda}^{(l-1)}. \quad (57)$$

If one treats each term in the above sum as a vector of length $\Omega(t_l - t_{l-1})$ pointing in the direction $\tilde{\rho}_a^{(l)}$, then placing the vectors end to end forms a *closed* figure, demonstrating the effective DC error suppression. In this picture, SK1 yields a triangle, whereas BB1 corresponds to two triangles with opposite signed area, indicating second-order correction, as expected [1].

Returning to the FF construction, we find that the amplitude-noise FF may be

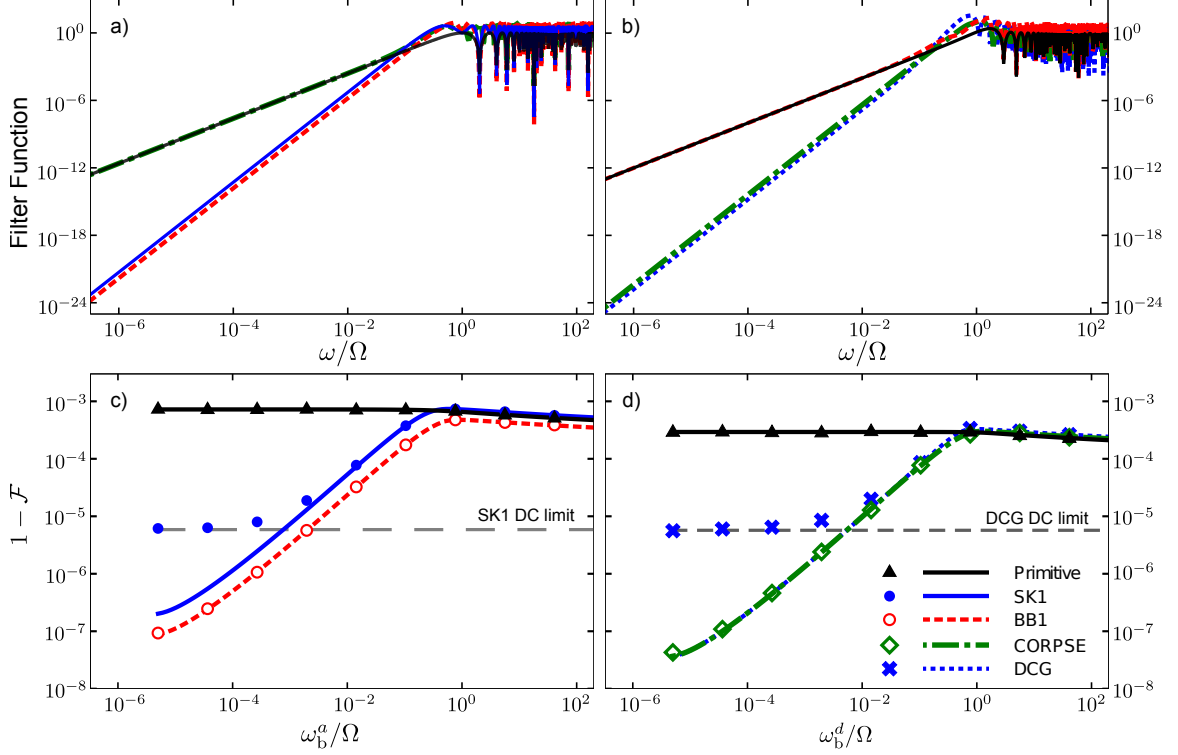


Figure 9: Top: FFs as a function of dimensionless frequency for amplitude [Panel a)], and detuning noise [Panel b)]. A target rotation angle $\theta = \pi$ is used for all sequences. Bottom: Performance of CP sequences in the presence of constant power amplitude [Panel c)] and detuning noise [Panel d)] with $1/f$ Gaussian noise spectrum and $1/f^2$ roll-off, Eq. (59). Spectrum parameters: $A_a = A_d \equiv A = 2.07 \cdot 10^9 / [\log(\omega_b/\omega_{\min}) + 1 - (\omega_b/\omega_{\max})]$ (rad/s)³/Hz, where ω_b is the knee of the roll-off; $\omega_{\min} = 2\pi$ rad/s, $\omega_{\max} = 4.5 \cdot 10^9$ rad/s. Control amplitude: $\Omega = 1.5 \cdot 10^6$ rad/s. Numerical simulation involves discretization of the continuous noise functions $\beta_\mu(t)$, calculating a single instance of $U(\tau, 0)$ and a single value for fidelity, and averaging over N noise realizations. We employ the Karhunen-Loeve filter [5] to simulate discrete noise in the Gaussian limit [6]. Analytical lines representing the fidelity loss calculated by the FF approach [Eq. (68), in color] and by the DC limit approach [Eq. (58), gray] are plotted. The DC limit for BB1 and CORPSE are below the bounds of the plot at $1 - \mathcal{F} = 3.9 \times 10^{-9}$ and $1 - \mathcal{F} = 3.0 \times 10^{-9}$, respectively

written as

$$F_a(\omega) = \frac{1}{4} \left\{ \left| \sum_l A_l(\omega) \tilde{\boldsymbol{\rho}}_a^{(l)} \right|^2 + \left| \sum_l B_l(\omega) \tilde{\boldsymbol{\rho}}_a^{(l)} \right|^2 \right\},$$

$$A_l(\omega) \equiv \cos(\omega t_l) - \cos(\omega t_{l-1}),$$

$$B_l(\omega) \equiv \sin(\omega t_l) - \sin(\omega t_{l-1}).$$

The above expression for $F_a(\omega)$ may be interpreted in terms of the magnitudes of two three-dimensional real vectors $\mathbf{A} \equiv \sum_l A_l(\omega) \tilde{\boldsymbol{\rho}}_a^{(l)}$ and $\mathbf{B} \equiv \sum_l B_l(\omega) \tilde{\boldsymbol{\rho}}_a^{(l)}$. When ω is small compared to the relevant time scales, Taylor-expansion of B_l shows that to second order in ω , we have $\sum_l B_l(\omega) \tilde{\boldsymbol{\rho}}_a^{(l)} \approx \frac{\omega}{\Omega} \sum_l \Omega(t_l - t_{l-1}) \tilde{\boldsymbol{\rho}}_a^{(l)} = 0$, which corresponds to (a scaled version of) the closed-loop condition required for error suppression at DC, Eq. (57). To second order, $A_l \approx \frac{\omega^2}{2}(t_l^2 - t_{l-1}^2)$, which thus dominates the error. This implies that all CPs for amplitude noise should have FFs that scale at least as ω^4 in the limit of small ω . These observations tie to previous knowledge about general FFs and associated error-suppressing properties [46, 4].

Fig. 10 shows the vectors \mathbf{A} and \mathbf{B} divided by ω (dashed green arrows corresponding to B_l/ω and solid red arrows corresponding to A_l/ω , respectively) and placed end-to-end for SK1 and BB1, for two different values of the dimensionless frequency ω/Ω . At sufficiently small ω the dashed green arrows trace an approximate closed path, whereas for higher frequencies, $\omega \gtrsim 0.1 \Omega$, higher-order terms become important. In this case, the resulting figure is no longer closed and the sequence will not be error-suppressing, in agreement with the FF analysis presented above. Thus, this geometric picture reflects common observations for DC error analyses, but now lifted to a time-dependent error model, analyzed in the frequency domain.

We can also use the small ω limit of \mathbf{A} and \mathbf{B} to estimate the crossover frequency at which the CP FF, $F_a^{CP}(\omega)$, will exceed the primitive pulse FF, $F_a^P(\omega)$. The primitive pulse FF is determined by the leading term in \mathbf{B} , $F_a^P(\omega) \approx \frac{1}{4}(\omega \tau_P)^2$, where τ_P is the pulse duration. The low frequency CP FF is determined by the leading term in \mathbf{A} ,

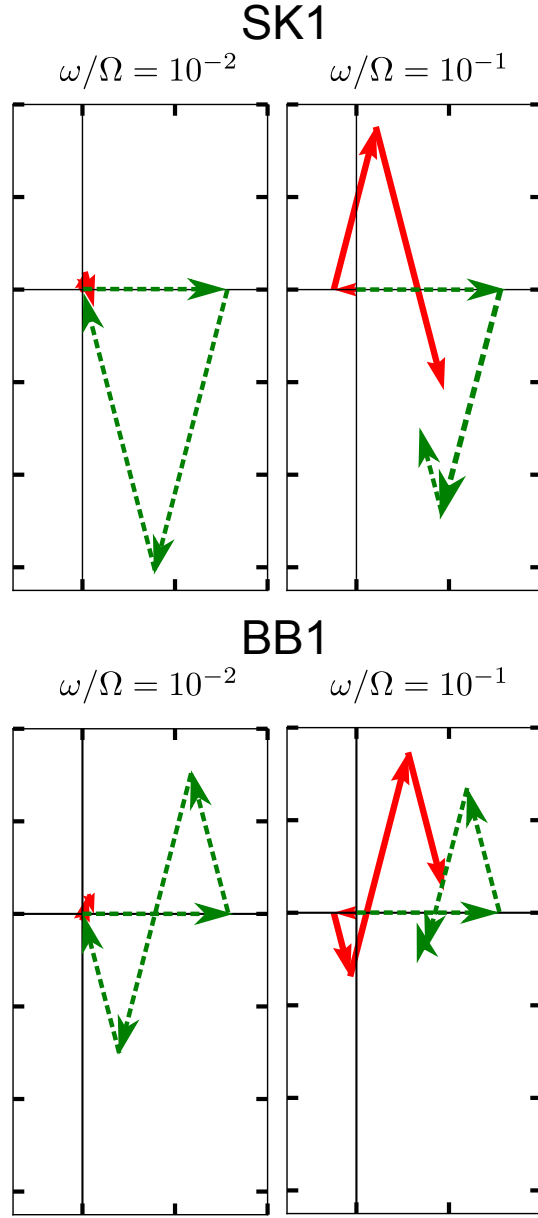


Figure 10: Geometric picture for first- vs. second-order amplitude-error CPs. The axes represent Cartesian x and y , indicating the rotation axes of the different segments [see text]. The initial rotation is about the x -axis, indicated by the horizontal line, with corrections about different axes conducted subsequently. Returning to the origin indicates suppression of error, with two different time-domain elements of the FF being indicated by color (dashed green/solid red).

which can be bounded from above by making the assumption that all $\tilde{\rho}_a^{(l)}$ are the same. This results in $F_a^{CP} = \frac{1}{16}(\omega\tau_{CP})^4$, where τ_{CP} is the length of the composite pulse. For SK1 and BB1 with $\theta = \pi$, $\tau_{CP} = (4\pi + \theta)/\Omega$ and this bound predicts that the composite pulse will reduce the error, $F_a^{CP}(\omega) < F_a^P(\omega)$, when $\omega < 0.025\Omega$. This is an approximate lower bound; the actual crossover frequencies are $\omega = 0.069\Omega$ for SK1 and $\omega = 0.127\Omega$ for BB1.

3.2.3 DC limit

While the approaches described in previous subsection capture the effects of a dynamic bath well, the first-order FF formalism underestimates error in the region $\omega/\Omega \ll 1$, corresponding to noise processes fluctuating slowly on the scale of operation time. This may be understood by treating very slow noise as a constant error term equal to the strength of H_{err} at the start of the sequence, $\beta_\mu(0)$. For small, constant noise an m -th order CP (or DCG) sequence is well approximated by $U^{[m]}(\tau, 0) \approx U_0(\tau, 0) \exp[-i\Phi_{m+1}(\tau)]$, where $\Phi_{m+1}(\tau)$ is the $(m+1)$ th order term in the perturbative Magnus expansion [3, 1]. For a qubit as we consider, $\Phi_{m+1}(\tau)$ is traceless with eigenvalues $\pm\lambda_{m+1}$ and the magnitude of λ_{m+1} is proportional to $\beta_\mu(0)^{m+1}$. The fidelity of the sequence is then $\mathcal{F} \approx \langle \cos(\lambda_{m+1})^2 \rangle$. In this limit, the leading order error term can thus be written as

$$1 - \mathcal{F} \approx \langle \lambda_{m+1}^2 \rangle = c_{m+1} \langle \beta_\mu(0)^{2(m+1)} \rangle, \quad (58)$$

where the proportionality constant c_{m+1} , like $F_\mu(\omega)$, depends on the sequence and the noise axis, but not the noise strength.

As an example, consider SK1 with constant noise $\beta_a(0)$. The leading-order Magnus term is

$$\begin{aligned} \Phi_2(\tau) &= i \frac{\beta_a(0)^2}{2} \int_0^\tau dt \int_0^t dt' [\rho_a(t), \rho_a(t')] \\ &= \beta_a(0)^2 \pi^2 \sin(2\phi_1) \sigma_z \end{aligned}$$

where $\phi_1 = \cos^{-1}(-1/4)$ (see Table 1). The eigenvalues of Φ_2 are $\pm\lambda_2 = \pm\beta_a(0)^2\pi^2\sin(2\phi_1)$ and as a result $1 - \mathcal{F} \approx (\pi^2\sin(2\phi_1))^2\langle\beta_a(0)^4\rangle$. The term $c_2 = (\pi^2\sin(2\phi_1))^2$ depend only the pulse sequence and $\langle\beta_a(0)^4\rangle$ is averaged over the ensemble of initial noise strengths.

The error of the first-order fidelity approximation in the FF formalism [Eq. (68)] only depends on the first-order Magnus term [Eq. (20)], so the slow-noise (DC) limit contains fidelity loss contributions from higher-order FF terms that are ignored in the first-order approximation (see also [4] for additional details). For a zero mean Gaussian noise described by a spectral density $S(\omega)$, by definition $\langle\beta_\mu(0)^2\rangle = \int_{-\infty}^{\infty} d\omega S_\mu(\omega)$. All odd orders of the expectation value are zero and all even orders are proportional to powers of the second order expectation value,

$$\langle\beta_\mu(0)^{2(m+1)}\rangle = (2m+1)!! \left(\int_{-\infty}^{\infty} d\omega S_\mu(\omega) \right)^{m+1}.$$

We may therefore estimate the analytical fidelity loss over the entire frequency range by combining the contributions from Eq. (68) and Eq. (58).

3.2.4 Comparison with numerical results

Quantifying the fidelity loss [Eq. (68)] for control protocols implemented in a real (classical) noise environment requires one to choose a specific noise spectrum. As a practical example, we consider $1/f$ Gaussian noise with a roll-off to $1/f^2$ noise at high frequency with spectrum (see Fig. 8)

$$S_\mu(\omega) = \begin{cases} A_\mu/\omega, & \omega_{\min}^\mu < \omega < \omega_{\text{b}}^\mu, \\ \omega_{\text{b}}^\mu \cdot A_\mu/\omega^2, & \omega_{\text{b}}^\mu < \omega < \omega_{\max}^\mu, \\ 0 & \text{otherwise,} \end{cases} \quad (59)$$

where A_μ is a constant amplitude for the two error quadratures $\mu \in \{a, d\}$. This type of noise is frequently encountered in experimental qubit systems over a wide frequency range [94, 95, 33] and naturally arises from independent bistable fluctuators [96]. The

generality of this power spectrum in various noise processes allows us to reasonably assume the same power spectrum for both amplitude and detuning noise, despite the fact that these two noise sources have different physical origins in general and, as remarked, we take them to be independent. Nonetheless we emphasize that our methods are independent of the specific form of the power spectrum assumed in our numerical calculations.

We analytically compute the fidelity loss according to Eq. (68) in combination with the asymptotic error floor, Eq. (58). These analytic results are compared to numerical data obtained from simulation of the Bloch vector evolution under the noisy Hamiltonian in Eq. (19). Provided that the number of noise realizations, N , over which we average is large enough, this numeric simulation can be considered a reliable direct method for calculating the fidelity. In fact, numeric results for fidelity loss converge after averaging over $N \simeq 10^4$ noise realization. We perform a quick analysis of fidelity distributions for primitive gate, SK1 and BB1 CPs. For the noisy X -rotation that for primitive gate can be represented as $M(\theta) = R(\theta) \cdot R(\varepsilon)$ (where ε is an over- or under rotation angle), the fidelity loss (Eq. (21)) scales as

$$1 - \mathcal{F} = 1 - \left\langle \cos^2 \left(\frac{\varepsilon}{2} \right) \right\rangle. \quad (60)$$

While the random values of ε follow the Gaussian distribution, the numerical fidelity loss will be distributed according to Eq. (60). In the Fig. 11 we demonstrate the distributions for ε and deviations of fidelity loss calculated numerically for 1000 random samples of the noise. Corresponding distributions of numerical fidelity loss for SK1 and BB1 are shown in Fig. 12. As we can observe, the SK1 fidelity loss, comparing to BB1 protocol, is distributed over a wider range of values.

For the three first-order protocols studied (SK1, CORPSE, and DCG), the lower panels of Fig. 9 show that as the roll-off frequency is reduced, the fidelity loss is well approximated by the combination of the FF estimate and DC limit (lines). Vitally,

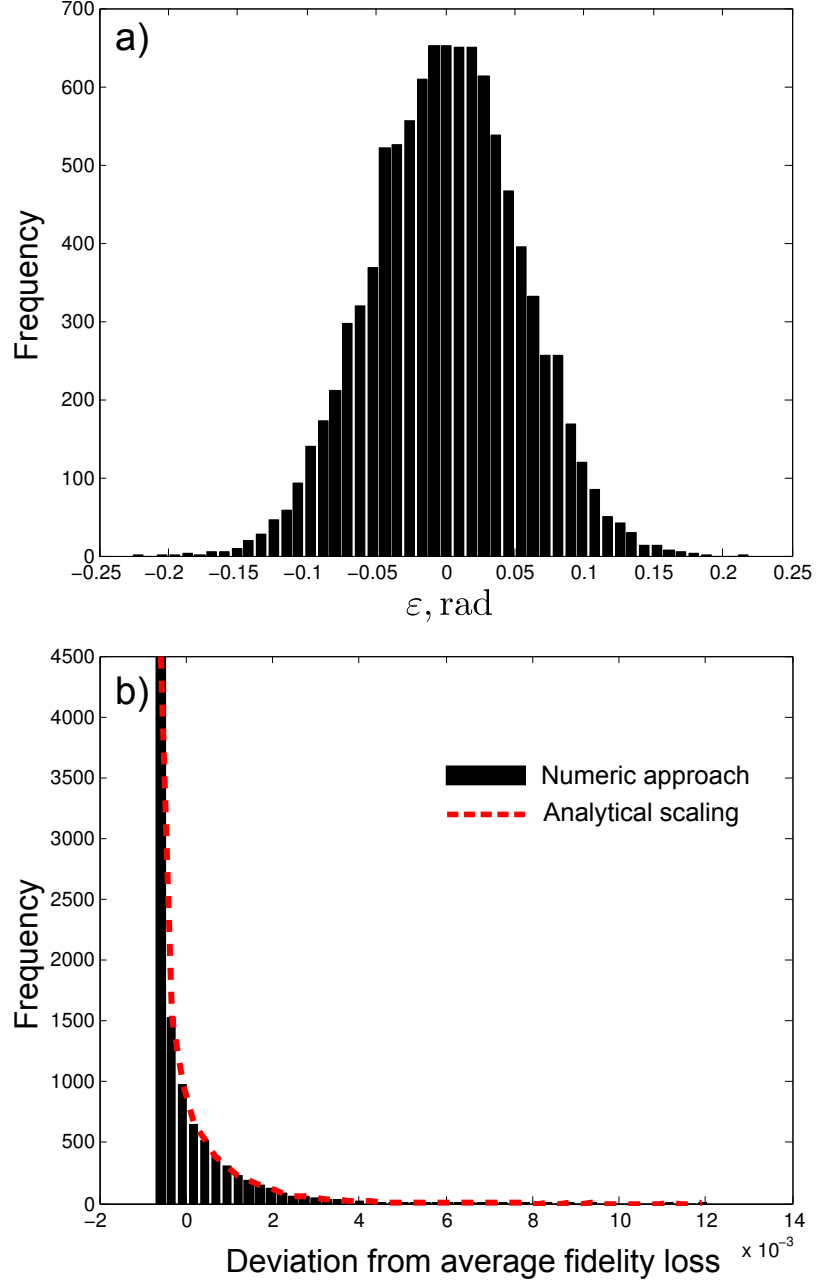


Figure 11: (a) Distribution of an angle of error rotation, ε (see text), based on 1000 samples of numeric noise realizations for primitive X -gate. (b) Distribution of deviations of fidelity loss for primitive X -gate. Black bars correspond to numeric calculations and red dashed line corresponds to Eq. (60).

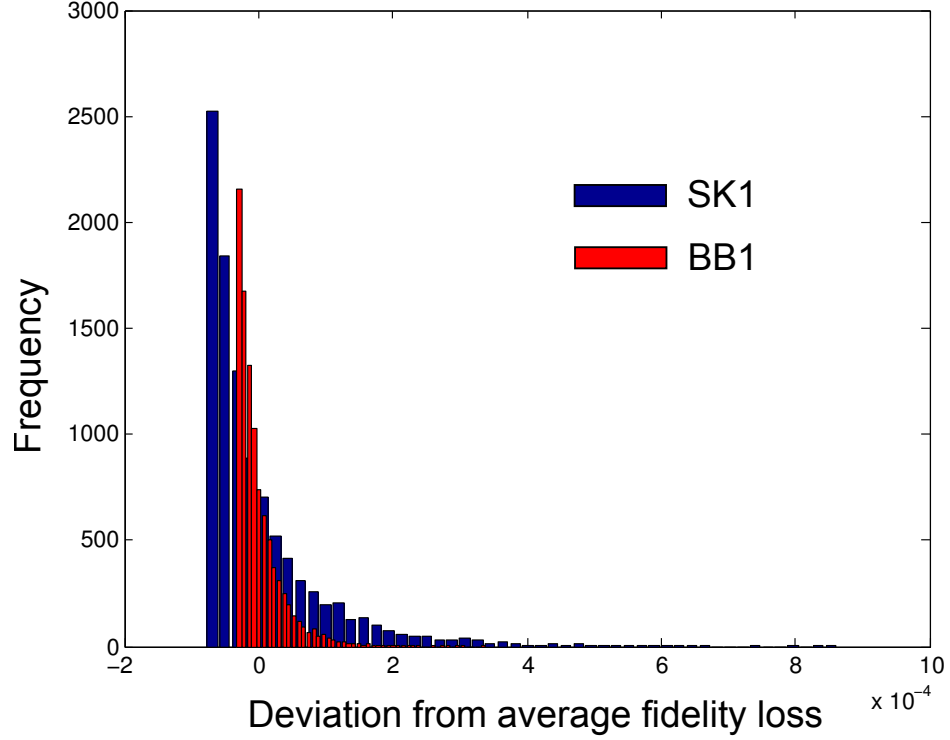


Figure 12: Distributions for fidelity loss deviations based on 1000 samples of numeric noise realizations for BB1 and SK1 CP sequences.

both the analytic and numerical approach directly reveal the robustness of CP protocols against noise fluctuations up to $\sim 0.1\Omega$. Detailed performance variation in the slow-noise limit stems from differences in construction of the selected gate protocols. The DCG and CORPSE sequences both correct DC detuning noise to the first order and have first-order FF's for time-dependent errors. While for frequencies below $\sim 10\%$ of the Rabi frequency the DCG has a FF of lower magnitude than CORPSE, the specific CORPSE sequence used is designed to additionally minimize the residual second-order DC pre-factor [1] (namely, c_2 in Eq. (58)), which results in a DC limit of X well below the plotted fidelities. The resulting relative performance between the DCG and CORPSE protocols further depends on the specifics of the noise power spectral density. Similarly, the effective second-order DC error cancellation associated with BB1 means that the DC-limit does not provide a substantial contribution relative to the FF calculation for the example noise spectrum.

Finally, we extend our analysis to include representative concatenated CP sequences (Table 1). We see that the FFs of the concatenated CP sequences depicted in Fig. (13) exhibit error suppression for both forms of error at low frequencies relative to a primitive pulse, in contrast to the standard CP sequences. In the presence of simultaneous noise, this leads to substantially improved performance when both noises are slow. Fig. 14 and Fig. 15 present a quantitative comparison of analytical and numerical fidelity-loss calculations for the primitive π -pulse and for reduced CinBB, showing good agreement between the two approaches. For this two-parameter compensating sequence, the constant-error DC fidelity limit may be seen to arise due to a cross-term of the two noise sources, namely,

$$1 - \mathcal{F} = c_{1,1} \langle \beta_a(0)^2 \beta_d(0)^2 \rangle,$$

where $c_{m+1,n+1}$ is the cross-term equivalent of c_{m+1} for single noise sources in Eq. (58). As the data show, the resulting DC limit matches the fidelity loss in the very low frequency regime for the reduced CinBB sequence.

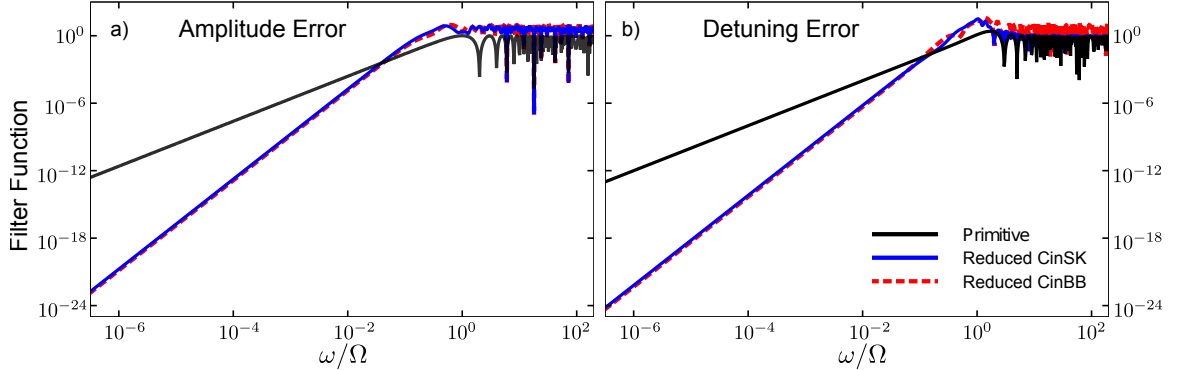


Figure 13: FFs as a function of dimensionless frequency for amplitude error [Panel a)] and detuning error [Panel b)] for concatenated CP sequences Reduced CinSK and Reduced CinBB. Unlike SK1, BB1, CORPSE, and DCG (see Fig. 9), these FFs scale as ω^4 for both errors.

Our numerical calculations validate the insights provided by the analytic FF formalism and demonstrate that, in combination with the calculated DC error floor, the first-order FF is an effective tool for predicting single-qubit control performance in the

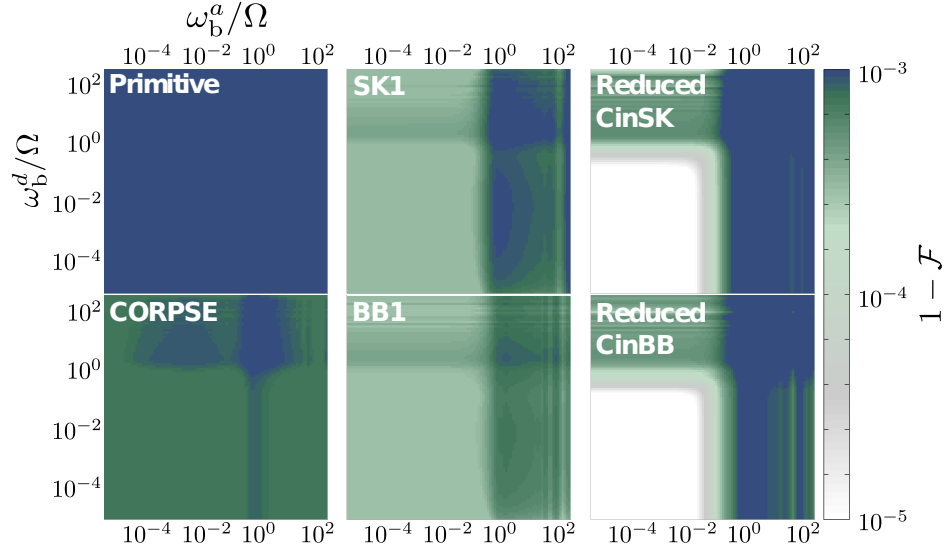


Figure 14: Performance of CPs under simultaneous amplitude and detuning noise, as a function of dimensionless frequency roll-off from $1/f$ to a $1/f^2$ spectral density, ω_b^a and ω_b^d , respectively. Spectrum and control parameters as in Fig. 9. Analytical results for fidelity loss. For each point the FF and DC limit calculations are compared and the larger fidelity loss value is plotted.

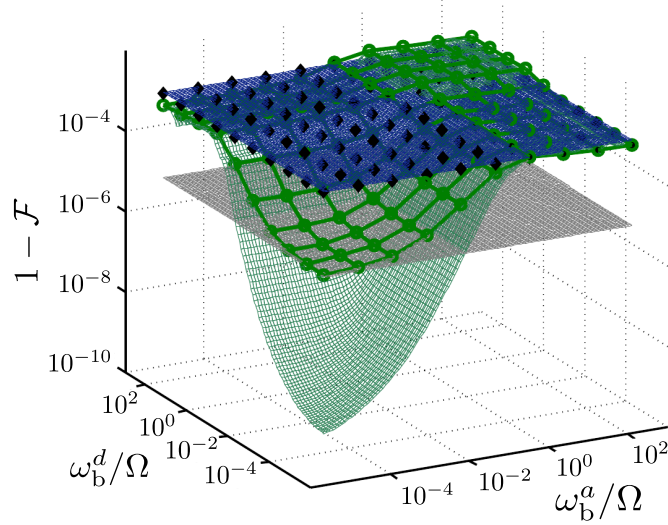


Figure 15: Performance of Reduced CinBB under simultaneous amplitude and detuning noise, as a function of dimensionless frequency roll-off from $1/f$ to a $1/f^2$ spectral density, ω_b^a and ω_b^d , respectively. Spectrum and control parameters as in Fig. 9. Analytical (FF: green surface, DC-limit: gray surface) and numerical results (green circles and mesh) for Reduced CinBB vs. analytical (DC-limit: blue surface) and numerical results (black diamonds) for a primitive pulse.

presence of time-dependent noise. The analytic approach comes with an additional benefit, however, in terms of computational efficiency; the numerical calculations of fidelity loss under time-dependent noise are in fact significantly more computationally intensive than the FF approach. While this is beyond our current purpose, such an advantage is likely to become even more dramatic in more complex control scenarios, in particular including multiple qubits.

3.3 Trapezoidal pulses

In actual experiments, pulse shape deviates from the ideal square-pulses under which CPs are derived. This is often done on purpose when, for example, Gaussian pulses or Blackman pulses are used to limit the spectral bandwidth of the control [97, 98]. This also occurs accidentally due to bandwidth limitations of the instrument resulting in fast amplitude fluctuations or slow turn off times. Although the FF formalism as described in previous sections assumes piecewise-constant control, continuous pulse-modulation profiles can be analyzed by a discrete time step approximation. We apply this approximation to examine the effect of pulse shape on CP FFs for amplitude and detuning noise.

We expect that the FF of amplitude noise CPs will be weakly dependent on pulse shape since amplitude noise, unlike detuning noise, commutes with the control pulse. In fact, using the error model of Eq. (19), the FF is pulse-shape independent if the total pulse time is the same as the square pulse it replaces. CPs for amplitude noise were developed assuming the error is proportional to the control (multiplicative noise). This noise can be modeled in our formalism by replacing $\beta_a(t)$ in Eq. (19) with $\Omega_l/\Omega_{\max}\beta_a(t)$. We note that additive and multiplicative error models are equivalent for the constant Ω pulses considered in the main text. In the case of multiplicative noise, static error correction only requires the rotation angle be constant. On the other hand, detuning noise does not commute with the control and as a result the

pulse shape can have a significant effect.

As an example, we examine trapezoidal pulses where the k -th pulse is ramped up to Ω_k in a time r , held for a time w , and then ramped down in a time r . The total pulse time is $w + 2r$ and $w + r$ is held constant to preserve the rotation angle. For the CPs studied here, $\Omega_k = \Omega$. BB1 and SK1 are designed assuming a systematic and proportional error in the rotation angle. This is preserved for multiplicative amplitude noise, and we see that the FF form is maintained (Fig. 16). There is an increase in the magnitude of the FF in the small ω region due to the increase in the overall sequence length in time.

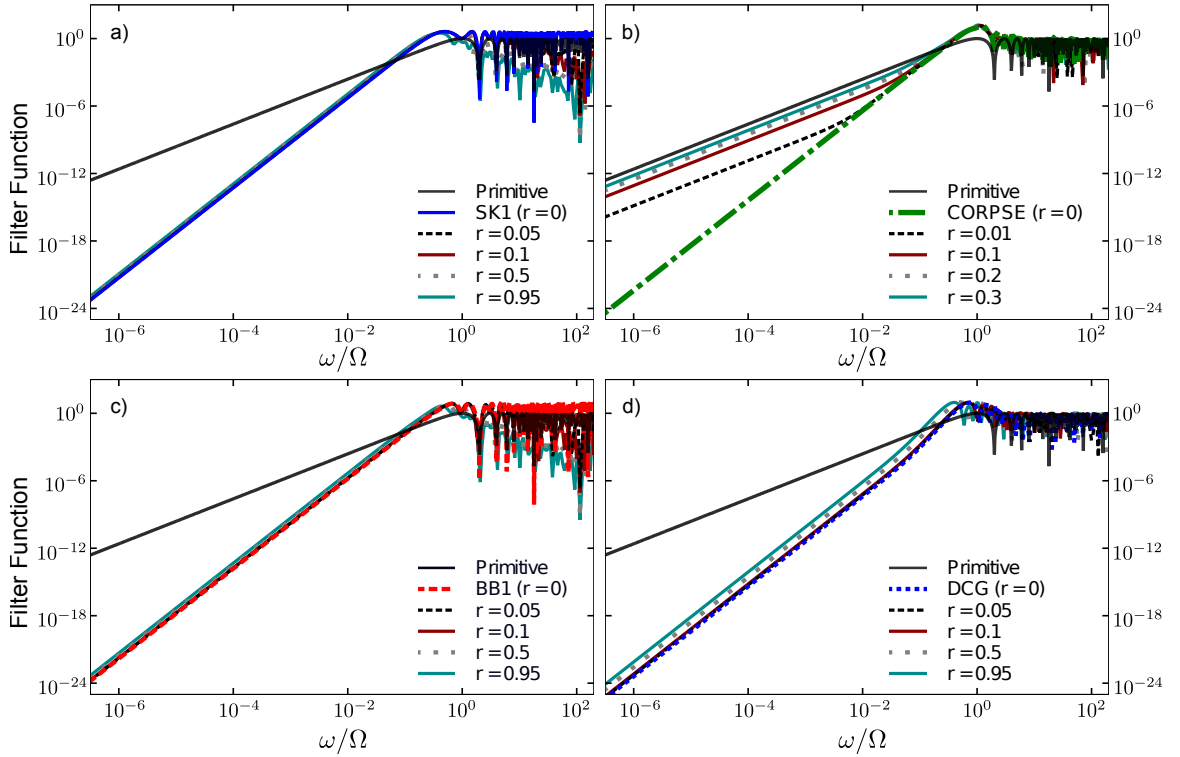


Figure 16: FFs as a function of dimensionless frequency for SK1 [Panel a)] and BB1 [Panel c)] in the presence of multiplicative amplitude noise and for CORPSE [Panel b)] and DCG [Panel d)] in the presence of detuning noise. The CPs are constructed from trapezoidal pulses with ramp time r in units of π/Ω .

CORPSE is designed under the assumption of square pulses and the detuning is additive. Consequently trapezoidal pulses do not perfectly remove the first-order

error using the rotation angles of CORPSE. This changes the asymptotic behavior of the FF and we see a bend corresponding to the residual ω^2 term due to imperfect error cancellation (Fig. 16b). The bend occurs at lower frequencies as the control approaches a square profile.

In contrast, the design of π DCG does not assume square pulses [3]. The static error cancellation will occur if the first and the third pulse have the same time-dependent control profile applied for a total time T and the second pulse has the stretched and scaled control profile applied for time $2T$. The parameters for the first and second trapezoidal pulses are related as follows: $2r_1 = r_2$, $2w_1 = w_2$, and $\Omega_1/2 = \Omega_2$. The FF form at small ω remains unchanged and the magnitude again increases with overall sequence length (Fig. 16d).

In practice, if square pulses are not an adequate approximation, then CORPSE should not be used. Instead a DCG should be chosen or one can derive a CORPSE-like sequence using soft pulses to achieve similar slow-noise cancellation [99].

3.4 *Conclusion*

In this chapter we have shown that CP sequences originally designed to compensate only for static control errors may be successfully employed for non-Markovian time-dependent control and/or environmental errors as well. Our numeric and analytic results demonstrate that these sequences are robust against noise fluctuations up to $\sim 10\%$ of the control frequency, a surprisingly high value.

CHAPTER IV

OPTIMIZED PULSE SEQUENCES THAT ACT AS NOTCH FILTERS

In previous chapter, we examined the robustness of CP sequences and DCGs that were designed for static noise in the presence of time-dependent noise. We observed how the performance depended on the bend frequency where a broad spectral density transforms from a $1/f$ to a $1/f^2$ frequency dependence. A key tool for this analysis was the filter-transfer function (FF) formalism [45, 4, 50]. The roll-off frequency of the first-order FF was a good indicator of the maximum frequency of the frequency bend. We also saw the limits for the first-order formalism where for a very slow noise the FF approach underestimated the error and a pure DC approximation yielded more reliable estimates.

One advantage of the FF formalism is that the error can be estimated by an integral of the FF with the spectral density. Soare et al. [50] use this to design pulses using an optimization procedure which minimizes the area under the first-order FF alone. This method suppresses all slow noise processes irregardless of the spectral density and is robust for noise sources with relatively shapeless spectral densities.

For the case of spectral densities with sharp features, the integral of the first-order FF with the spectral density is a more appropriate target for minimization. In this Chapter we demonstrate that optimizing on this approximate fidelity yields results that are confirmed to be effective by direct numeric integration. Specifically we examine a noise model corresponding to a strong and narrow Gaussian peak on a broad $1/f$ background with a roll-off to $1/f^2$. Furthermore, the first-order FF yields insight into the pulse robustness with respect to changes in the position of

the Gaussian peak. We employ the method of simulated annealing [82] and GRAPE algorithm [64, 74, 80] in optimization routines.

4.1 Noise model

The system that we consider is a single qubit in the presence of a non-Markovian noise representing an error in either the detuning or amplitude of the control. In both scenarios, the noise spectrum is dominated by a strong Gaussian-shape peak added on top of a weak $1/f$ background with a roll-off to $1/f^2$:

$$S(\omega) = \begin{cases} S_g(\omega) + A_p/\omega, & \omega_{\min} < \omega < \omega_b, \\ S_g(\omega) + A_r/\omega^2, & \omega_b < \omega < \omega_{\max}, \\ 0, & \text{otherwise,} \end{cases} \quad (61)$$

where

$$S_g(\omega) = A_g \exp[-(\omega_0 - \omega)^2/2\sigma^2]. \quad (62)$$

The spectrum parameters are chosen in a way that $S_g(\omega)$ corresponds to a narrow strong peak. Example of this type of spectrum is presented in the fig. 17 and example of corresponding noise trajectories is presented in the fig 18.

For a sequence of n operations, amplitude noise $\beta_a(t)$ and detuning noise $\beta_d(t)$, both zero-mean Gaussian stationary processes, are introduced into the Hamiltonian as follows:

$$H_a(t) = \sum_{l=1}^n G^{(l)}(t) \frac{[\Omega_l + \beta_a(t)]}{2} \boldsymbol{\rho}^{(l)} \cdot \boldsymbol{\sigma}, \quad (63)$$

$$H_d(t) = \sum_{l=1}^n G^{(l)}(t) \frac{\Omega_l}{2} \boldsymbol{\rho}^{(l)} \cdot \boldsymbol{\sigma} + \beta_d(t) \sigma_z. \quad (64)$$

Here, $\boldsymbol{\sigma} \equiv (\sigma_x, \sigma_y, \sigma_z)$, are the Pauli operators. The function $G^{(l)}(t) \equiv \Theta[t - t_{l-1}] \Theta[t_l - t]$ has unit value for $t \in [t_{l-1}, t_l]$ and takes zero value otherwise. Each rotation characterized by control-field amplitude Ω_l and the axis $\boldsymbol{\rho}^{(l)} \equiv \boldsymbol{\rho}(\phi_l) = (\cos \phi_l, \sin \phi_l, 0)$.

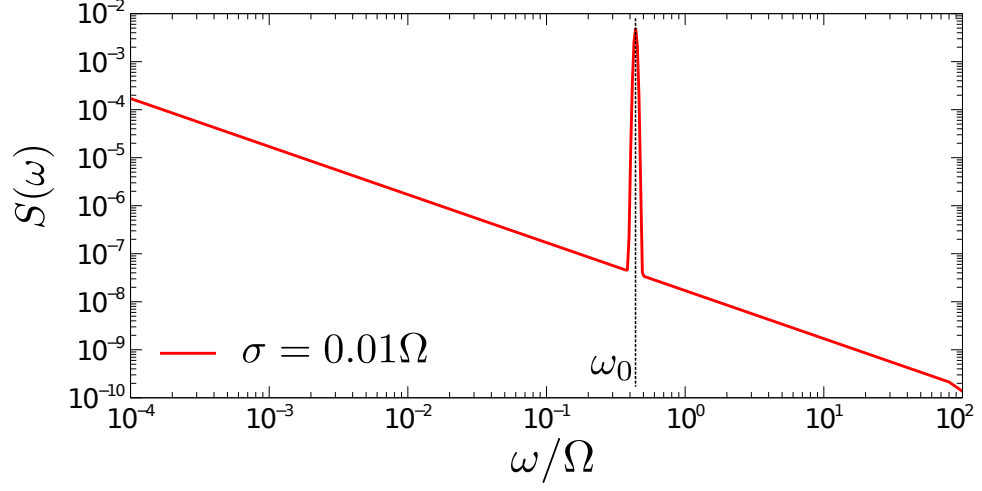


Figure 17: Example of considered power spectrum of Eq. (61) formed by Gaussian-shape peak with $\omega_0/\Omega \simeq 0.44$ (Eq. (62)) and $1/f$ background with a roll-off to $1/f^2$.

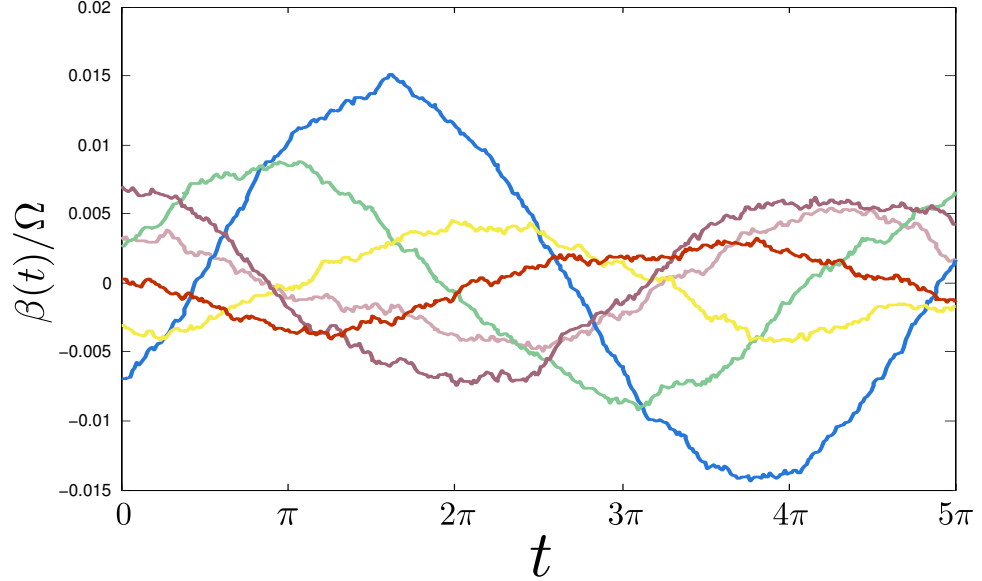


Figure 18: Example of noise trajectories for $\omega_0/\Omega \simeq 0.44$ corresponding to the spectrum of Eq. (61).

4.2 Control of amplitude noise

We employ several pulse sequence constructions a five-pulse model based on BB1 a CP for DC amplitude errors [18, 19] for arbitrary rotation angles and the F_1 5- π sequence developed by Jones [93] for π rotations. We assume each square pulse l has fixed Ω and we vary the time interval $[t_{l-1}, t_l]$ to change the rotation angle. For amplitude noise, the pulse shaping has minimal effect on the results if the total pulse time does not change [51].

In the BB1 type sequences, we modulate parameters α , β , ϕ_1 and ϕ_2 in the sequence

$$U_1 = R(\theta - \alpha, 0)R(\beta, \phi_1)R(2\pi, \phi_2) \times \\ \times R(2\pi - \beta, \phi_1)R(\alpha, 0). \quad (65)$$

It is constructed in a way that for each set of $\{\alpha, \beta, \phi_1, \phi_2\}$, U_1 is always equivalent to $R(\theta, 0)$ in a *noise-free* regime. Parameter α is constrained to interval $[0, \theta]$, while other parameters can take any value in $[0, 2\pi]$.

For F_1 type sequences [93], we sequentially perform an odd number n of operations $R(\pi, \phi_l)$, they result in a total rotation $R(\pi, \Phi)$, where $\Phi = \sum_l^n (-1)^l \phi_l$. In this study we limit this construction to $n = 5$ and $\Phi = 0$. Therefore, the sequence for $R(\pi, 0)$ can be written as

$$U_2 = R(\pi, \phi_5)R(\pi, \phi_4)R(\pi, \phi_3)R(\pi, \phi_2)R(\pi, \phi_1), \\ \phi_5 = \phi_4 - \phi_3 + \phi_2 - \phi_1, \quad (66)$$

and independent parameters to be modulated are ϕ_1, ϕ_2, ϕ_3 and ϕ_4 . The limitation of construction U_2 is that it only produces a π -rotation, while U_1 can be used for arbitrary rotations.

4.3 Control of detuning noise

The presence of detuning noise term in Hamiltonian of Eq. (64) leads to decoherence effects that can be potentially reduced if we vary control frequency $\{\Omega_l\}$. For this purpose we modulate control profile in a basis of Walsh functions, which are binary valued square-wave functions [100, 50, 88], and search for a sequence with the best performance for a given noise model. Rotation phase ϕ_l is limited to 0 or π with a default value of 0.

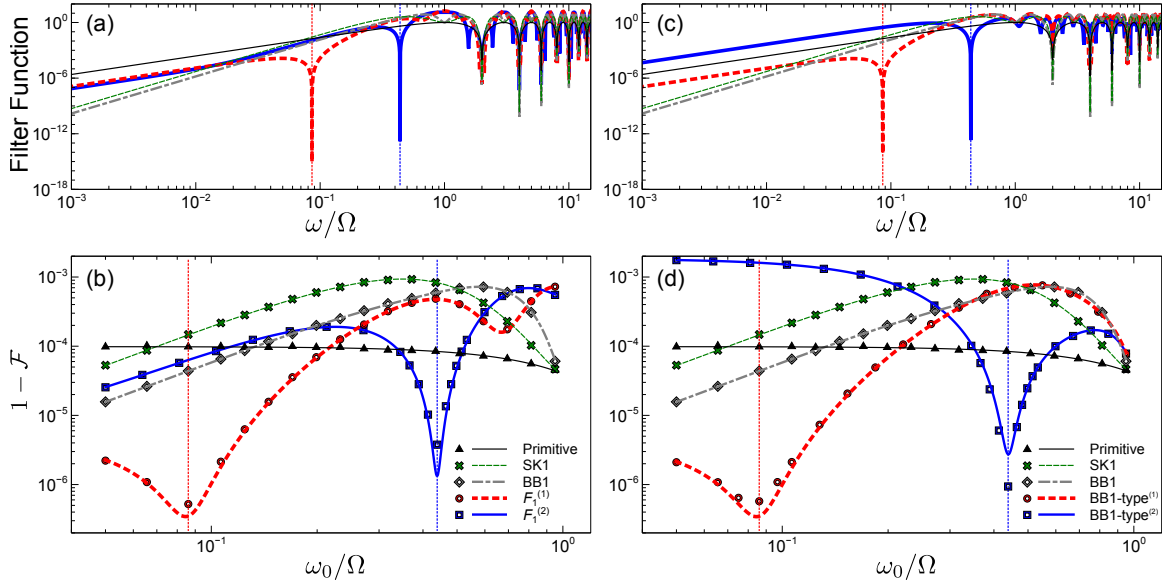


Figure 19: Top: FFs as a function of dimensionless frequency. Vertical dashed lines indicate target values of ω_0 for which control protocols based on Eq. (65) [Panel a)] and based on Eq. (66) [Panel c)] were synthesized. Bottom: Performance of quantum control protocols as a function of parameter ω_0/Ω for a Gaussian spectral peak including control protocols based on Eq. (65) [Panel b)] and based on Eq. (66) [Panel d)]. Analytical fidelity loss computed by the FF approach (lines) is compared to numerical simulations (markers).

Let us replace our discrete control vector $\{\Omega_l\}$ by continuous function $\Omega(t)$ defined such that it takes the value Ω_l for $t \in [t_{l-1}, t_l]$. We build the sequence power profile as the following linear combination $\Omega(t) = \sum_{k=0}^n X_k \text{PAL}_k(t/\tau)$, where $\text{PAL}_k(t/\tau)$ is a Walsh function of Paley order k , and τ is a total duration of the sequence. We are interested only in odd values of k and only in those Walsh functions which are

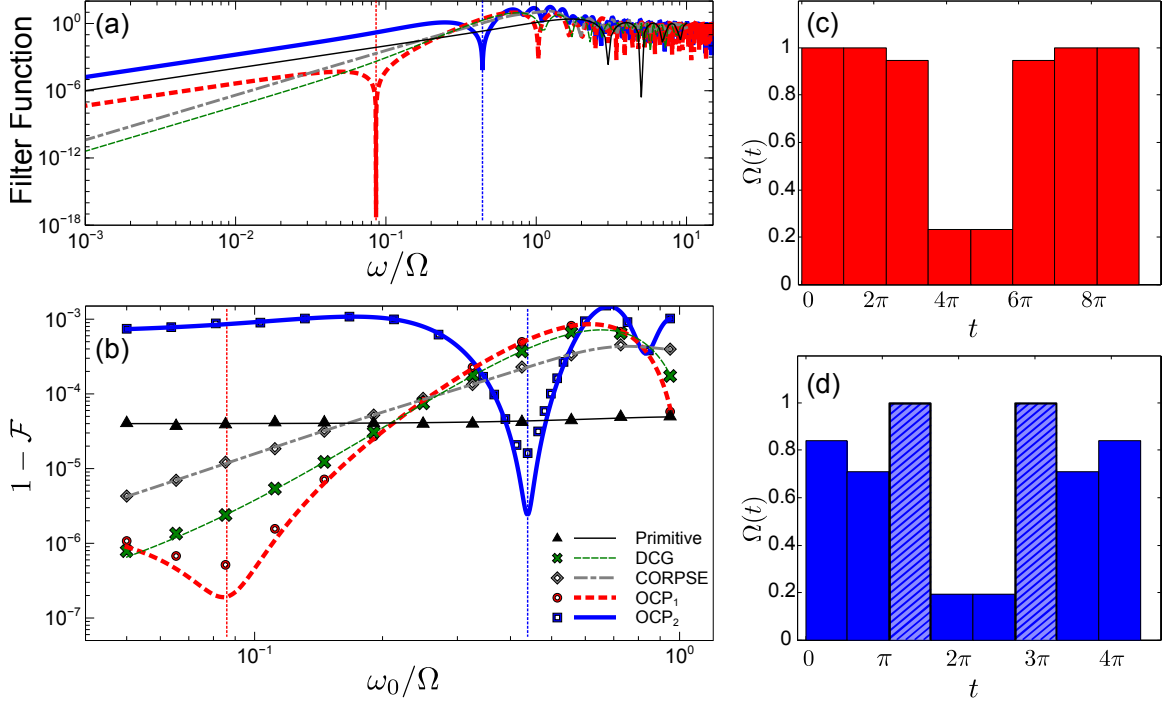


Figure 20: (a) FFs as a function of dimensionless frequency. Vertical dashed lines indicate target values of ω_0 for which OCP₁ and OCP₂ were synthesized. (b) Performance of quantum control protocols as a function of central frequency ω_0/Ω for a Gaussian peak in detuning spectrum. Analytical fidelity loss based on the FF approach (lines) is compared to numerical simulation (markers). Spectrum parameters: (c) Amplitude profile for OCP₁ synthesized from Walsh functions (d) Amplitude profile for OCP₂. Diagonal-line pattern of 3rd and 6th pulse corresponds to the rotation phase $\phi_1 = \phi_8 = \pi$ which equals 0 elsewhere.

symmetrical around the middle point of time axis. These conditions lead to the control search space which has been shown to be more effective [50]. For example, for 8-pulse sequence only the subset of $k = \{0, 3, 5, 6\}$ is included in the sum.

Due to periodic properties of Walsh functions only the first term, $X_0\text{PAL}_0(t/\tau) \equiv X_0$, defines the area under the curve $\Omega(t)$ and, consequently, the resulted rotation angle $\theta = X_0\tau$. So, by fixing X_0 , in a noise-free regime we generate a target gate regardless of values of X_3 , X_5 and X_6 . During modulation of these parameters we also perform a rescaling of τ to limit the maximum value of $\Omega(t)$ to 1, while the length of each pulse equals τ/n . If $\Omega(t)$ is negative for some operation, we take its absolute value and flip the phase from 0 to π .

4.3.1 Objective function and Optimization procedure

In both amplitude and detuning noise regimes, our goal is to design a sequence that would be maximally close to an ideal unitary U_0 in the presence of noise. The effect of the noise is captured by the average fidelity

$$\mathcal{F} = \frac{1}{4} \left\langle |\text{Tr}(U_0^\dagger V)|^2 \right\rangle, \quad (67)$$

where V is an actual propagator in the presence of single trajectory of stochastic process, and the brackets $\langle . \rangle$ denote the averaging over large ensemble of noise trajectories. The fidelity loss, $1 - \mathcal{F}$, can be chosen as an objective function that requires minimization.

One particular approach to fidelity loss is taken in FF formalism [45, 4], which has shown a potential use for fast evaluation of performance for composite pulses [51] (also, see previous chapter), and has been proven to be valid experimentally [50]. FF $F(\omega)$ captures the spectral characteristics of an arbitrary set of single-qubit operations and allows us to compare performance of different combinations of pulses by quantitative means.

Using the definition of noise power spectrum, $S(\omega) \equiv \int_{-\infty}^{\infty} dt e^{-i\omega t} \langle \beta(t_0) \beta(t_0 + t) \rangle$,

we give the expression for the first-order fidelity loss [4]:

$$1 - \mathcal{F} \approx \frac{1}{2\pi} \int_{-\infty}^{\infty} \frac{d\omega}{\omega^2} S(\omega) F(\omega). \quad (68)$$

With FF formalism we can easily calculate FFs for the sequence constructions described for amplitude and detuning noise in previous sections. Being expressed by analytical functions, the integral in Eq. (68) is a feasible measure of control performance and it can be easily implemented in our numeric optimization routine.

4.3.1.1 *Simulated annealing*

We have discussed various optimization methods in more details in Chapter II. In order to obtain notch-filter sequences we employ the method of simulated annealing [82] implemented in MATLAB package for quantum control [74]. It takes minutes to generate optimized solutions that can be considered as good approximations to global minima for both amplitude and detuning noise control settings.

For the control construction of Eq. (65), we vary the set of $\{\alpha, \beta, \phi_1, \phi_2\}$ and compute objective function of Eq. (68). For the sequence in Eq. (66) the varying controls are $\{\phi_1, \phi_2, \phi_3, \phi_4\}$. Finally, in the case of detuning noise control variables are coefficients, $\{X_3, X_5, X_6\}$, of the expansion in Walsh basis.

The particular cooling scheme for simulated annealing that we implement is defined as $T(t + \Delta t) = cT(t)$, where $c < 1$ (see fig. 6 for details).

4.3.1.2 *GRAPE algorithm*

We also employ the GRAPE algorithm [64, 74, 80] for amplitude noise to compare the resulted sequences to the constructions specified above. In contrast to the BB1-type and F_1 -type sequences where the control power Ω_l is fixed to 1, in GRAPE optimization we modify it from pulse to pulse. Therefore, we also need to take into account the multiplicative nature of the amplitude noise, and the Hamiltonian of Eq.

(63) will take the form

$$H_a(t) = \sum_{l=1}^n G^{(l)}(t) \frac{\Omega_l[1 + \epsilon(t)]}{2} \sigma_{\phi_l}. \quad (69)$$

Here $\epsilon(t)$ represents a multiplicative control noise which is related to $\beta_a(t)$ by $\beta_a(t) = \Omega_l \cdot \epsilon(t)$. In the case of fixed control power, $\epsilon(t)$ and $\beta_a(t)$ are formally equivalent.

In the GRAPE implementation, the variable controls are components $u_x^{(l)}$ and $u_y^{(l)}$ of applied power along σ_x and σ_y :

$$H_a(t) = \sum_{l=1}^n G^{(l)}(t) \frac{1}{2} \{u_x^{(l)}[1 + \epsilon(t)]\sigma_x + u_y^{(l)}[1 + \epsilon(t)]\sigma_y\}. \quad (70)$$

Two forms of Hamiltonian in Eq. (69) and Eq. (70) are equivalent if we relate $u_x^{(l)}$ and $u_y^{(l)}$ to control power, Ω_l , and rotation phase, ϕ_l , by $\Omega_l = \sqrt{(u_x^{(l)})^2 + (u_y^{(l)})^2}$ and $\tan \phi_l = u_y^{(l)} / u_x^{(l)}$.

While in simulated annealing we evaluate the objective function by the means of FF formalism, in GRAPE routine we calculate the average fidelity numerically using Eq. (67) and the resulting objective function is averaged over multiple numerical noise realizations. In order to generate the optimized sequences that way, we have modified GRAPE implementation in QuTiP (Quantum Toolbox in Python) software [101, 102]. In particular, we have added a support for the presence of stochastic noise in control power. In this case, the objective function is computed as an ensemble-averaged control performance.

4.4 Results

4.4.1 Amplitude noise

We present optimized notch-filter sequences for two different peak frequencies of amplitude control noise. Results based on simulated annealing are given in the Fig. 19, where we compare them to standard pulses (SK1 and BB1 [19, 18]) and to primitive π -rotation. In terms of FFs (top panels of Fig. 19) synthesized composite pulses clearly demonstrate resonance behavior for the target frequencies (marked by vertical

lines). In the bottom panels of Fig. 19 fidelity loss is calculated as a function of a peak location in frequency domain. Performance of new sequences are significantly better than that of SK1, BB1 and primitive gate for a certain frequency range around the spectral peak.

In the fig. 21, we present GRAPE pulse sequences optimized for target frequency $\omega_0/\Omega = 0.439$. We compare these sequences to the pulses considered above and primitive pulses of two types. Due to multiplicative character of amplitude noise, it can be advantageous to apply pulses with a low power but longer durations. Therefore, additionally to the original primitive π -pulse, we demonstrate the performance of ‘slow’ π -pulse where Ω is fixed to 0.2. In the panels (c) and (d) of the fig. 21 we show GRAPE profiles for 5 and 10 pulses respectively. It is clear that 10-pulse sequences demonstrate better performance as these control protocols have more flexible structure.

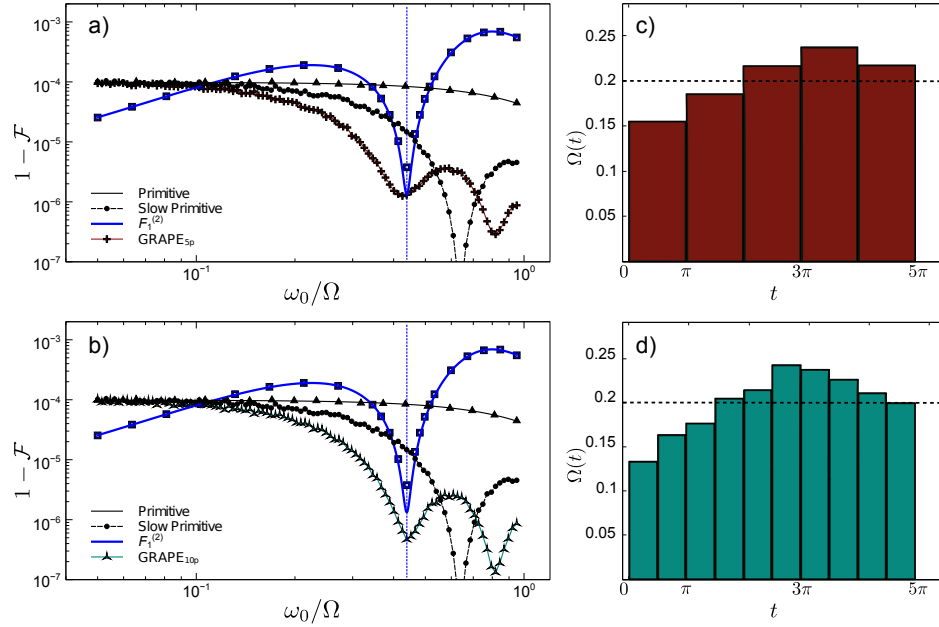


Figure 21: Performance of GRAPE pulse sequences optimized for $\omega_0 \simeq 0.44$ with 5-pulse structure (a) and 10-pulse structure (b). Control power profiles are given on panels (c) and (d), respectively. Dashed Horizontal lines denote ‘slow’ π -pulse. Fidelity loss for the F_1 -type pulse sequence (Fig 19) is given for comparison.

We do not present results from GRAPE algorithm applied for a ‘slow’ sharp peak ($\omega_0/\Omega \simeq 0.08$) that we considered for simulated annealing. We observe that GRAPE is not effective for time-dependent noise with slow dynamics due to existence of multiple local minima on this control landscape.

4.4.2 Detuning noise

On the left panels of Fig. 20 we demonstrate FFs and the performance for control protocols based on simulated annealing for the case of detuning noise. Optimized notch-filter sequences with control profiles on the right panels of Fig. 20 are also designed for particular frequencies of a spectral peak, they are compared to standard pulses such CORPSE [18, 92] and DCG for X -gate [3, 4]. Again, notch-filter behavior of FFs leads to advantage in performance in target range of frequencies. One can also note that new pulse sequences for a slower frequency peak are more effective than those which correct for fast frequency noise.

4.5 Conclusion

In this chapter we have demonstrated a possibility to obtain numerically single-qubit pulse sequences optimized for particular target frequency of present noise. These sequences act as notch filters which suppress a strong narrow peak in a noise spectrum. We compare performance of optimized control protocols to standard CPs and to dynamically-corrected gates designed for slow non-Markovian noise. As it is expected, standard protocols are outperformed by optimized sequences for the given noise model. We can conclude that this approach would help to reduce a noise effect on the qubit system provided that the noise oscillations have a dominant frequency.

CHAPTER V

COMPOSITE PULSES FOR SINGLE-QUBIT GATES IN A SURFACE ELECTRODE ION TRAP

This chapter describes our recent work that has been done in collaboration with the research group of Professor Jungsang Kim at Duke University. The study by E. Mount et al. [7] considers experimental work on error compensation of single-qubit gates in a surface electrode ion trap using composite pulses [7]. Here we discuss our theoretical contributions to the simulation of randomized benchmarking protocols that have been used to measure gate errors. In these protocols, various composite pulse sequences have been employed for compensation of introduced amplitude error, and in this way, recently developed compact palindromic pulse compensation sequences [23] have been shown to be effective against high-amplitude errors. We present details on randomized benchmarking technique and the structure of pulse sequence simulations.

5.1 Experimental methods

Among quantum computer architectures the trapped atomic ion qubits successfully demonstrate key properties such as long coherence times [103], high accuracy of qubit measurement [104], and possibility to implement a set of universal logic gates [105]. The fidelity of quantum gates on trapped ion qubits has been limited by the stability of the control fields used to manipulate the states of ion. In practice, the logic gates based on microwave fields [106, 28, 107] provide gate fidelities several orders of magnitude higher than those using laser fields [108, 109, 110]. In this work, the low-error single-qubit gates performance is demonstrated by using stimulated Raman

transitions on an ion qubit trapped in a microfabricated chip trap. In order to measure the gate errors a randomized benchmarking protocol [108, 111, 112] has been employed. The randomized benchmarking technique is discussed in more details in the next section. Amplitude errors in the control beam were suppressed by composite pulses to the extent predicted by our numeric simulations. It has been shown that the single-qubit gates based on BB1 CP sequence [1] can have an average error per randomized Clifford group gate as low as $3.6(3) \cdot 10^{-4}$. It is also demonstrated in experiment that PD6 CP sequence designed by G. H. Low et al. shows an expected high-order error compensation.

In microfabricated surface electrode ion traps atomic ions are trapped above a two dimensional surface of electrodes. This device is a very promising platform for a scalable quantum computer [113, 114].

In the experiment that we consider, the states of a qubit have been encoded in two hyperfine ground states $|0\rangle = {}^2S_{1/2}|F = 0, m_f = 0\rangle$ and $|1\rangle = {}^2S_{1/2}|F = 1, m_f = 0\rangle$ of the $^{171}\text{Yb}^+$ ion (Fig. 22). The energy separation between these two states corresponds to $f_{\text{qubit}} = 12.6\text{GHz}$, and it is relatively insensitive to the possible magnetic field fluctuations. For Raman transitions, they have used picosecond pulses from a mode-locked titanium-sapphire (Ti-Sapph) laser doubled to a center frequency of 376 nm, which creates combs in the frequency domain with comb teeth spacing equal to the laser repetition rate ($f_{\text{rep}} \simeq 76\text{ MHz}$). The frequency doubler output is split into two nearly co-propagating frequency combs using a single acousto-optic modulator driven with modulation frequencies f_1 and f_2 , demonstrated in Fig. 23. Resonant transitions are driven by pairs of optical frequency comb teeth (2 and 3 in Fig. 23), one from each comb, with a frequency difference equal to f_{qubit} [115, 116] (see [7] for details).

For each experiment, the ion is first Doppler cooled for 1 *ms* using light that is red-detuned from ${}^2S_{1/2}|F = 1\rangle \rightarrow {}^2P_{1/2}|F = 0\rangle$ resonance. The qubit is then initialized

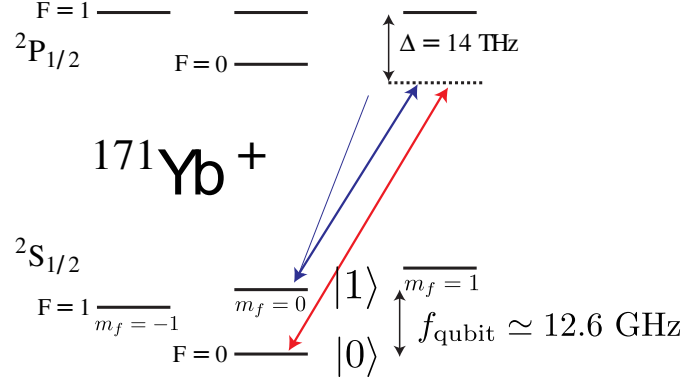


Figure 22: Relevant energy levels used in the $^{171}\text{Yb}^+$ ion. Adapted from [7].

to the $|0\rangle$ state. In order to measure the qubit state, they use a light resonant with $^2S_{1/2}|F=1\rangle \rightarrow ^2P_{1/2}|F=0\rangle$ transition turned on for $400\ \mu\text{s}$ and measure the ion fluorescence by a photo-multiplier tube (PMT). The fluorescence would correspond to the $|1\rangle$, and the absence of fluorescence (a dark state) would correspond to the $|0\rangle$ state.

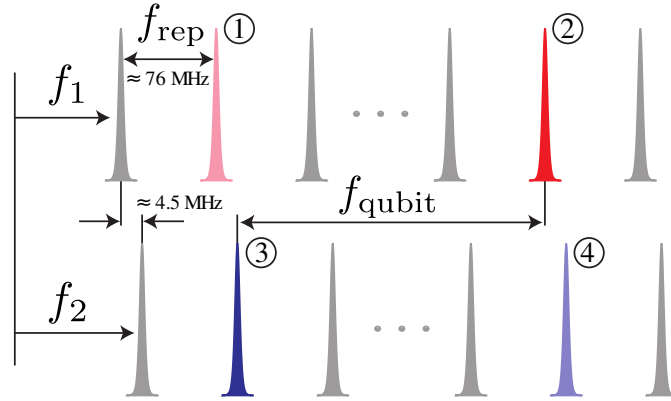


Figure 23: Relevant optical frequency combs. Adapted from [7].

In the described experiment, the impact of residual systematic amplitude errors in the Raman beams was suppressed through the use of CP sequences. Since the CPs (see Chapter III) are usually designed to work on systematic errors that are constant over the duration of the sequence, the sequence length determines the bandwidth below which the effect of fluctuating error is suppressed. The length of most CPs increases rapidly at higher error correction order. The palindromic pulse sequences

(PDn) are unique in that they scale linearly with the corrected error order (to $n = 12$) [23]. Here we analyze the use of BB1 [1] and PD6 [23] CPs and their ability to correct for static amplitude errors in the presence of additional phase and timing errors for Clifford group gates.

In order to efficiently characterize the average error of single-qubit gates we employ the randomized benchmarking technique which is discussed in more details below.

5.2 *Randomized benchmarking*

A major requirement for quantum computing realizations is to implement low-error logical gates. Namely, the error probability should be of the order of 10^{-4} [54]. It is very hard to measure such low errors in experiments and one approach to that is to use process tomography to determine the properties of quantum operations [54]. The limitations of this technique is that it does not necessarily provide a complete information about quantum gate behavior for the wide range of situations. For example, the process tomography does not necessarily determine how well a particular gate would perform as the element of a sequence of logical operations. But more importantly, these techniques do not allow to separate the effects of SPAM (state preparation and measurement) errors from the intrinsic gate errors. An alternative method, randomized benchmarking was proposed by E. Knill *et al.* [108] in 2008 and was inspired by using randomization to analyze quantum noise [117]. It later found a wide use in quantum computing [111, 112].

We consider the randomized benchmarking method in application for one qubit. In this case, the qubit is first initialized to the $|0\rangle$ state. Then a large number of experiments is performed that consist of an alternating sequence of either π -pulses or identity operations (Pauli randomization) and $\pi/2$ -pulses (considered as computational gates) chosen at random. All these rotations are in Clifford group [111] (see Table 2) and the qubit state is always an eigenstate of a Pauli operator. All sequences

are followed by a final Clifford gate which brings the final qubit state to either $|0\rangle$ or $|1\rangle$, at random. The qubit is then being measured in computational basis and compared to the state which is expected in a noise-free regime.

The randomization ensures that the measurement outcome is not correlated with any pulse sequences or with any particular operations. Typically, the length l of a randomized pulse sequence is referred to the number of $\pi/2$ -pulses in the sequence. The role of π -pulses is only to randomize the error by changing the Pauli frame [108]. If we perform N experiments for each length $l = 1, \dots, L$ and measure the error probability p_l for each experiment, we can estimate a single pulse error rate. Then the average fidelity loss per pulse can be obtained from relationship between p_l and l . While we refer to original sources [108, 112] for details, we discuss the basic steps of randomized benchmarking protocol:

- 1) Choose and fix a sequence length L and generate K_L random sequences each consisting of uniformly distributed Clifford elements. Overall, there are $L+1$ quantum operation in each sequence, where L is a number of random Clifford gates and the last $(L+1)$ th operation returns the qubit state to z -basis.

- 2) For each of the K_L sequences, obtain the survival probability measured by comparing the final qubit state to the expected state.

- 3) Obtain averaged sequence fidelity by averaging over all K_L random realizations.

- 4) For different values of L , repeat operations 1) - 3) to obtain averaged survival probability $\mathcal{F}_{seq}(L)$ per gate length calculated as the fraction of events where measurement outcomes match the expected results. Then fit the averaged survival probability to the following model (this model corresponds to the case of gate-independent and time-independent errors [112])

$$\mathcal{F}_{seq}(L) = A_0 p^L + B_0, \quad (71)$$

where p is related to the average error per Clifford gate r through $r = (1 - p)/2$, and A_0 and B_0 correspond to the SPAM errors and the error on the final rotation. The

derivation of the model Eq. (71) can be found here [112].

5.3 *Experimental results and numeric simulation*

In the case of considered experiment [7], for each sequence length L there were 20 random sequences. Each sequence was measured 800 times for calculating of averaged survival probability. By fitting it to the model Eq. (71), average error per gate and associated uncertainty have been obtained. The effective amplitude error was introduced by changing the Raman beam duration for each pulse. Therefore, the rotation angle was changed from θ to $\theta(1 + \epsilon)$ (See previous chapters for amplitude noise models). The lowest error per gate $3.6(3) \cdot 10^{-4}$ was observed by translating each individual rotation into a BB1 CP at an amplitude error of $\epsilon = 0.2$. Correcting the amplitude error for each pulse using BB1 reduced the gate error by 67% from the lowest measured uncompensated gate error $1.1(2) \cdot 10^{-3}$.

In order to compare the experimental results to numerical calculations, we designed a simulation program that includes error due to the presence of non-resonant comb teeth pairs and a non-static timing error. We simulated the exact sequences used in the experiments in the presence of different types of noise.

In Fig. 24 we present a comparison of the error from primitive gates and BB1 and PD6 pulse sequences as a function of amplitude error. Our simulations qualitatively reproduce the agreement with experimental data for both BB1 and PD6 sequences. However, in experiment the best performance at suppressing amplitude noise is demonstrated by BB1 sequence, since the PD6 is a longer sequence and it is more sensitive to the additional errors caused by off-resonant Raman transitions.

5.4 *Conclusion*

In this chapter, we discuss a work which reports high fidelity single qubit gates driven with tightly focused laser beams on trapped ion qubits by laser intensity stabilization and use of compensating pulse sequences. An error probability as low as $3.6(3) \cdot$

10^{-4} is demonstrated, consistent with error levels required for realizing a range of quantum error-correction schemes. We discuss the theoretical modeling that was used to compare experimental data to numeric simulations.

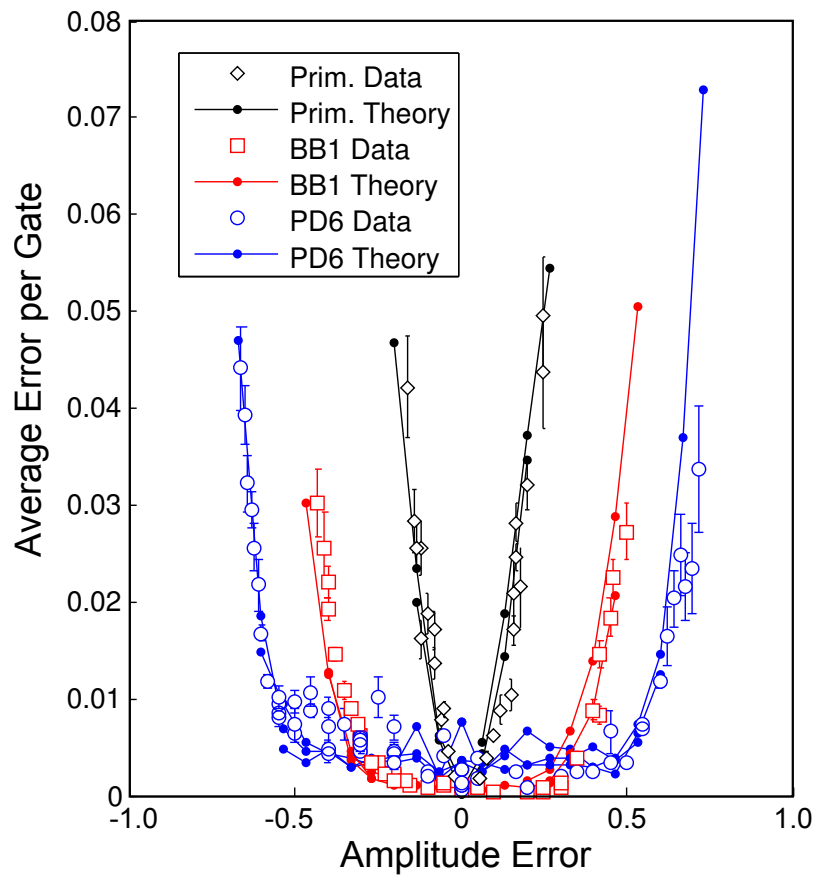


Figure 24: Single qubit gate error degradation with systematic amplitude error.

Table 2: The Clifford group gates written as the physical gates applied.

Clifford gate	Physical gates
1	I
2	X
3	Y
4	Z
5	X/2
6	Y/2
7	Z/2
8	-X/2
9	-Y/2
10	-Z/2
11	Z & X/2
12	X/2 & Z
13	Z/2 & X
14	X & Z/2
15	Z/2 & X/2
16	Y/2 & Z/2
17	X/2 & -Z/2
18	Y/2 & Z
19	-X/2 & Z/2
20	-Z/2 & Y/2
21	Z & Y/2
22	-Z/2 & X/2
23	X/2 & Z/2
24	-Y/2 & -Z/2

CHAPTER VI

CONCLUSION

In this work, we present a systematic study of pulse sequences for single-qubit control in the presence of time-dependent noise. In addition to substantially expanding the practical significance of open-loop quantum control protocols, our analysis further establishes the utility of FFs as a unifying and computationally efficient framework for estimating and understanding the performance of coherent control protocols under realistic noise spectra. Furthermore, we have shown that at least for the single-qubit setting under consideration, slow noise can be accurately modeled by a DC-limit approximation that can be combined with the FF approach to accurately estimate control performance over a broader frequency range.

Altogether, our results show that, in combination, CP and DCG protocols provide experimentalists with a viable toolkit capable of meeting a variety of constraints, including the presence of colored time-dependent control noise.

We further notice that the geometric picture we have developed, in conjunction with the FF approach, may prove instrumental for finding new CPs which are resilient to specific noise spectra.

We have demonstrated this possibility by developing new pulse sequences that act as notch filters. It is a demonstrative example that the overlap integral of the first-order FF with the spectral density can serve as an effective target for performance error minimization. We expect that these methods together with broad approaches currently developed in quantum information community can further advance the field of quantum control. Particularly with respect to time-dependent noise, the question of a robust suppressing of arbitrary broad noise spectrum remains open.

APPENDIX A

NUMERICAL NOISE SIMULATION

In this work we have used numerical simulations for stochastic processes to confirm our theoretical findings and derivations. In this Appendix we discuss a technique of Karhunen-Lo  ve (KL) filter for modeling a noise process with a given autocorrelation function $R(t)$ as a set of discrete numerical sequences [5]. This method is designed to generate a wide-sense stationary Gaussian noise. For this type of noise the correlation function is related to the power spectral density by the Wiener-Khinchin theorem [55]:

$$\begin{aligned} S(\omega) &= \int_{-\infty}^{\infty} dt e^{-i\omega t} R(t) \\ R(t) &= \int_{-\infty}^{\infty} dt e^{i\omega t} S(\omega). \end{aligned}$$

The output of KL filter is a numerical noise vector, \mathbf{z} , with a correlation matrix defined in a discrete way as

$$\langle z_i z_j \rangle = R(|j - i| \cdot \delta_t) \equiv A_{ij},$$

where δ_t is a discrete time step. The correlation matrix A is a positive semi-definite Toeplitz matrix since correlation function, $R(t)$, is a real, symmetric function [85]. Therefore, Toeplitz matrix can be diagonalized by a real orthogonal matrix M :

$$A = M \Lambda M^T,$$

here Λ is a non-negative diagonal matrix. We can denote it by Λ_j .

Now we can generate noise trajectories as

$$z_i = M_{ij} \sqrt{\Lambda_j} x_j,$$

where x_j is an element of a zero-mean vector \mathbf{x} formed based on normal distribution. This vector can be easily by a computer program.

We can check that $\{z_i\}$ has a required autocorrelation characteristics by calculating the expected mean $\langle z_i \rangle$ and expected autocovariance $\langle z_i z_j \rangle$:

$$\begin{aligned}
\langle z_i \rangle &= M_{ij} \sqrt{\Lambda_j} \langle x_j \rangle = 0; \\
\langle z_i z_j \rangle &= \sum_{m,n} M_{im} \sqrt{\Lambda_m} M_{jn} \sqrt{\Lambda_n} \langle x_m x_n \rangle = \\
&= \sum_{m,n} M_{im} \sqrt{\Lambda_m} M_{jn} \sqrt{\Lambda_n} \delta_{mn} = \\
&= \sum_m M_{im} \sqrt{\Lambda_m} M_{jm} = \\
&= (M \Lambda M^\top)_{ij} = \\
&= A_{ij}.
\end{aligned}$$

As we can see, the noise vector \mathbf{z} has a given spectral characteristics and can be used to simulate Gaussian noise with arbitrary autocorrelation function.

REFERENCES

- [1] MERRILL, J. T. and BROWN, K. R., “Progress in compensating pulse sequences for quantum computation,” *Advances in Chemical Physics*, vol. 154, pp. 241–294, 2014.
- [2] BANDO, M., ICHIKAWA, T., KONDO, Y., and NAKAHARA, M., “Concatenated composite pulses compensating simultaneous systematic errors,” *J. Phys. Soc. Jpn.*, vol. 82, p. 014004, 2013.
- [3] KHODJASTEH, K. and VIOLA, L., “Dynamically error-corrected gates for universal quantum computation,” *Phys. Rev. Lett.*, vol. 102, p. 080501, 2009.
- [4] GREEN, T. J., SASTRAWAN, J., UYS, H., and BIERCUK, M. J., “Arbitrary quantum control of qubits in the presence of universal noise,” *New Journal of Physics*, vol. 15, 2013.
- [5] GHANEM, R. G. and SPANOS, P. D., *Stochastic Finite Elements: A Spectral Approach*. Springer London, Limited, 2012.
- [6] KASDIN, N. J., “Discrete simulation of colored noise and stochastic processes and 1/f alpha; power law noise generation,” *Proceedings of the IEEE*, vol. 83, pp. 802–827, 1995.
- [7] MOUNT, E., KABYTAYEV, C., CRAIN, S., HARPER, R., BAEK, S., VRIJSEN, G., FLAMMIA, S., BROWN, K. R., MAUNZ, P., and KIM, J., “Error compensation of single-qubit gates in a surface electrode ion trap using composite pulses,” *arXiv:quant-ph/ 1504.01440*, 2015.
- [8] DOWLING, J. P. and MILBURN, G. J., “Quantum technology: The second quantum revolution,” *Philosophical Transactions of the Royal Society A: Mathematical, Physical and Engineering Sciences*, vol. 361, pp. 1655–1674, 2003.
- [9] WARREN, W. S., RABITZ, H., and DAHLEH, M., “Coherent control of quantum dynamics: The dream is alive,” *Science*, vol. 259, pp. 1581–1589, 1993.
- [10] BUTKOVSKII, A. G. and SAMOILENKO, Y. I., “Control of quantum systems,” *Automat. Rem. Control*, vol. 40, pp. 485–502, 1979.
- [11] BUTKOVSKII, A. G. and SAMOILENKO, Y. I., “Control of quantum systems (ii),” *Automat. Rem. Control*, vol. 40, pp. 629–645, 1979.
- [12] BUTKOVSKII, A. G. and SAMOILENKO, Y. I., “On the theory of control of observable quantum systems,” *Automat. Rem. Control*, vol. 44, pp. 178–188, 1983.

- [13] HUANG, G. M., TARN, T. J., and CLARK, J. W., “On the controllability of quantum-mechanical systems,” *Journal of Mathematical Physics*, vol. 24, pp. 2608–2618, 1982.
- [14] CHU, S., “Cold atoms and quantum control,” *Nature*, vol. 416, pp. 206–210, 2002.
- [15] DONG, D. and PETERSEN, I. R., “Quantum control theory and applications: A survey,” *IET Control Theory and Applications*, vol. 4, pp. 2651–2671, 2010.
- [16] D’ALESSANDRO, D., *Introduction to quantum control and dynamics*. Hoboken, NJ: Taylor and Francis Ltd, 2007.
- [17] LEVITT, M. H. and FREEMAN, R., “Compensation for pulse imperfections in NMR spin-echo experiments,” *J. Magn. Reson.*, vol. 43, pp. 65–80, 1981.
- [18] WIMPERIS, S., “Broadband, narrowband, and passband composite pulses for use in advanced NMR experiments,” *J. Magn. Reson.*, vol. 109, pp. 221 – 231, 1994.
- [19] BROWN, K. R., HARROW, A. W., and CHUANG, I. L., “Arbitrarily accurate composite pulse sequences,” *Phys. Rev. A*, vol. 70, p. 052318, 2004.
- [20] SOUZA, A. M., ÁLVAREZ, G. A., and SUTER, D., “Robust dynamical decoupling for quantum computing and quantum memory,” *Phys. Rev. Lett.*, vol. 106, p. 240501, 2011.
- [21] ODEDRA, S., THRIPPLETON, M. J., and WIMPERIS, S., “Dual-compensated antisymmetric composite refocusing pulses for nmr,” *Journal of Magnetic Resonance*, vol. 225, pp. 81–92, 2012.
- [22] TOMITA, Y., MERRILL, J. T., and BROWN, K. R., “Multi-qubit compensation sequences,” *New Journal of Physics*, vol. 12, 2010.
- [23] LOW, G. H., YODER, T. J., and CHUANG, I. L., “Optimal arbitrarily accurate composite pulse sequences,” *Phys. Rev. A*, vol. 89, p. 022341, 2014.
- [24] LEIBFRIED, D., BLATT, R., MONROE, C., and WINELAND, D., “Quantum dynamics of single trapped ions,” *Rev. Mod. Phys.*, vol. 75, pp. 281–324, 2003.
- [25] HÄFFNER, H., ROOS, C., and BLATT, R., “Quantum computing with trapped ions,” *Phys. Rep.*, vol. 469, pp. 155–203, 2008.
- [26] TIMONEY, N., ELMAN, V., GLASER, S., WEISS, C., JOHANNING, M., NEUHAUSER, W., and WUNDERLICH, C., “Error-resistant single-qubit gates with trapped ions,” *Phys. Rev. A*, vol. 77, p. 052334, 2008.
- [27] RAKREUNGDET, W., LEE, J. H., LEE, K. F., MISCHUCK, B. E., MONTANO, E., and JESSEN, P. S., “Accurate microwave control and real-time diagnostics of neutral-atom qubits,” *Phys. Rev. A*, vol. 79, p. 022316, 2009.

- [28] SHAPPERT, C. M., MERRILL, J. T., BROWN, K. R., AMINI, J. M., VOLIN, C., DORET, S. C., HAYDEN, H., PAI, C. S., BROWN, K. R., and HARTER, A. W., “Spatially uniform single-qubit gate operations with near-field microwaves and composite pulse compensation,” *New Journal of Physics*, vol. 15, 2013.
- [29] MERRILL, J. T., DORET, S. C., VITTORINI, G., ADDISON, J. P., and BROWN, K. R., “Transformed composite sequences for improved qubit addressing,” *Physical Review A - Atomic, Molecular, and Optical Physics*, vol. 90, 2014.
- [30] MORTON, J. J. L., TYRYSKIN, A. M., ARDAVAN, A., PORFYRAKIS, K., LYON, S. A., and BRIGGS, G. A. D., “High fidelity single qubit operations using pulsed electron paramagnetic resonance,” *Phys. Rev. Lett.*, vol. 95, p. 200501, 2005.
- [31] CHIORESCU, I., NAKAMURA, Y., HARMANS, C. J. P. M., and MOOIJ, J. E., “Coherent quantum dynamics of a superconducting flux qubit,” *Science*, vol. 299, pp. 1869–71, 2003.
- [32] CLARKE, J. and WILHELM, F. K., “Superconducting quantum bits,” *Nature*, vol. 453, pp. 1031–42, 2008.
- [33] MARTINIS, J. M., NAM, S., AUMENTADO, J., LANG, K. M., and URBINA, C., “Decoherence of a superconducting qubit due to bias noise,” *Phys. Rev. B*, vol. 67, p. 094510, 2003.
- [34] MONTANGERO, S., CALARCO, T., and FAZIO, R., “Robust optimal quantum gates for josephson charge qubits,” *Physical Review Letters*, vol. 99, 2007.
- [35] KHODJASTEH, K., BLUHM, H., and VIOLA, L., “Automated synthesis of dynamically corrected quantum gates,” *Physical Review A - Atomic, Molecular, and Optical Physics*, vol. 86, 2012.
- [36] KOSUT, R. L., GRACE, M. D., and BRIF, C., “Robust control of quantum gates via sequential convex programming,” *Physical Review A - Atomic, Molecular, and Optical Physics*, vol. 88, 2013.
- [37] MÖTTÖNEN, M., DE SOUSA, R., ZHANG, J., and WHALEY, K. B., “High-fidelity one-qubit operations under random telegraph noise,” *Phys. Rev. A*, vol. 73, p. 022332, 2006.
- [38] CHEN, Z., BOHNET, J. G., WEINER, J. M., and THOMPSON, J. K., “General formalism for evaluating the impact of phase noise on bloch vector rotations,” *Physical Review A - Atomic, Molecular, and Optical Physics*, vol. 86, 2012.
- [39] WANG, X., BISHOP, L. S., BARNES, E., KESTNER, J. P., and SARMA, S. D., “Robust quantum gates for singlet-triplet spin qubits using composite pulses,” *Physical Review A - Atomic, Molecular, and Optical Physics*, vol. 89, 2014.

- [40] VIOLA, L. and LLOYD, S., “Dynamical suppression of decoherence in two-state quantum systems,” *Physical Review A - Atomic, Molecular, and Optical Physics*, vol. 58, pp. 2733–2744, 1998.
- [41] VIOLA, L., KNILL, E., and LLOYD, S., “Dynamical decoupling of open quantum systems,” *Physical Review Letters*, vol. 82, pp. 2417–2421, 1999.
- [42] SCHIRMER, S. G., “Lagrangian and hamiltonian methods for nonlinear control 2006 - proceedings from the 3rd ifac workshop,” *Lecture Notes in Control and Information Sciences*, vol. 366 LNCIS, 2007.
- [43] KHODJASTEH, K. and LIDAR, D. A., “Fault-tolerant quantum dynamical decoupling,” *Phys. Rev. Lett.*, vol. 95, p. 180501, 2005.
- [44] KHODJASTEH, K., LIDAR, D. A., and VIOLA, L., “Arbitrarily accurate dynamical control in open quantum systems,” *Phys. Rev. Lett.*, vol. 104, p. 090501, 2010.
- [45] KOFMAN, A. G. and KURIZKI, G., “Universal dynamical control of quantum mechanical decay: Modulation of the coupling to the continuum,” *Phys. Rev. Lett.*, vol. 87, p. 270405, 2001.
- [46] BIERCUK, M. J., DOHERTY, A. C., and UYS, H., “Dynamical decoupling sequence construction as a filter-design problem,” *Journal of Physics B: Atomic, Molecular and Optical Physics*, vol. 44, p. 154002, 2011.
- [47] KHODJASTEH, K., SASTRAWAN, J., HAYES, D., GREEN, T. J., BIERCUK, M. J., and VIOLA, L., “Designing a practical high-fidelity long-time quantum memory,” *Nature Communications*, vol. 4, 2013.
- [48] GREEN, T. J., UYS, H., and BIERCUK, M. J. *Phys. Rev. Lett.*, vol. 109, p. 020501, 2012.
- [49] SZWER, D. J., WEBSTER, S. C., STEANE, A. M., and LUCAS, D. M., “Keeping a single qubit alive by experimental dynamic decoupling,” *Journal of Physics B: Atomic, Molecular and Optical Physics*, vol. 44, p. 025501, 2011.
- [50] SOARE, A., BALL, H., HAYES, D., SASTRAWAN, J., JARRATT, M. C., MCLOUGHLIN, J. J., ZHEN, X., GREEN, T. J., and BIERCUK, M. J., “Experimental noise filtering by quantum control,” *Nature Physics*, vol. 10, pp. 825–829, 2014.
- [51] KABYTAYEV, C., GREEN, T. J., KHODJASTEH, K., BIERCUK, M. J., VIOLA, L., and BROWN, K. R., “Robustness of composite pulses to time-dependent control noise,” *Physical Review A - Atomic, Molecular, and Optical Physics*, vol. 90, 2014.
- [52] BRIF, C., CHAKRABARTI, R., and RABITZ, H., “Control of quantum phenomena: Past, present and future,” *New Journal of Physics*, vol. 12, 2010.

- [53] GILMORE, R., *Lie Groups, Lie Algebras, and Some of Their Applications*. Krieger Publishing Company, 1994.
- [54] NIELSEN, M. A. and CHUANG, I. L., *Quantum computation and quantum information*. Cambridge University Press, 2000.
- [55] PAPOULIS, A., *Probability, Random Variables, and Stochastic Processes*. McGraw Hill, 1984.
- [56] KHODJASTEH, K. and VIOLA, L., “Dynamical quantum error correction of unitary operations with bounded controls,” *Phys. Rev. A*, vol. 80, p. 032314, 2009.
- [57] PAZ-SILVA, G. A. and VIOLA, L., “General transfer-function approach to noise filtering in open-loop quantum control,” *Physical Review Letters*, vol. 113, 2014.
- [58] PAZ-SILVA, G. A. and VIOLA, L., “A General Transfer-Function Approach to Noise Filtering in Open-Loop Quantum Control,” *arXiv:quant-ph/1408.3836*, 2015.
- [59] ROLOFF, R., WENIN, M., and PTZ, W., “Optimal control for open quantum systems: Qubits and quantum gates,” *Journal of Computational and Theoretical Nanoscience*, vol. 6, pp. 1837–1863, 2009.
- [60] ZHU, W. and RABITZ, H., “Closed loop learning control to suppress the effects of quantum decoherence,” *Journal of Chemical Physics*, vol. 118, pp. 6751–6757, 2003.
- [61] SKLARZ, S. E., TANNOR, D. J., and KHANEJA, N., “Optimal control of quantum dissipative dynamics: Analytic solution for cooling the three-level system,” *Physical Review A - Atomic, Molecular, and Optical Physics*, vol. 69, pp. 053408–1, 2004.
- [62] HOHENESTER, U., “Optimal quantum gates for semiconductor qubits,” *Physical Review B - Condensed Matter and Materials Physics*, vol. 74, 2006.
- [63] JIRARI, H. and PUTZ, W., “Optimal coherent control of dissipative n-level systems,” *Physical Review A - Atomic, Molecular, and Optical Physics*, vol. 72, 2005.
- [64] KHANEJA, N., REISS, T., KEHLET, C., SCHULTE-HERBRÜGGEN, T., and GLASER, S. J., “Optimal control of coupled spin dynamics: Design of nmr pulse sequences by gradient ascent algorithms,” *Journal of Magnetic Resonance*, vol. 172, pp. 296–305, 2005.
- [65] SCHULTE-HERBRÜGGEN, T., SPRL, A., KHANEJA, N., and GLASER, S. J., “Optimal control for generating quantum gates in open dissipative systems,” *Journal of Physics B: Atomic, Molecular and Optical Physics*, vol. 44, 2011.

- [66] GRACE, M., BRIF, C., RABITZ, H., WALMSLEY, I. A., KOSUT, R. L., and LIDAR, D. A., “Optimal control of quantum gates and suppression of decoherence in a system of interacting two-level particles,” *Journal of Physics B: Atomic, Molecular and Optical Physics*, vol. 40, pp. S103–S125, 2007.
- [67] KATZ, G., RATNER, M. A., and KOSLOFF, R., “Decoherence control by tracking a hamiltonian reference molecule,” *Physical Review Letters*, vol. 98, 2007.
- [68] GRACE, M. D., BRIF, C., RABITZ, H., LIDAR, D. A., WALMSLEY, I. A., and KOSUT, R. L., “Fidelity of optimally controlled quantum gates with randomly coupled multiparticle environments,” *Journal of Modern Optics*, vol. 54, pp. 2339–2349, 2007.
- [69] PALAO, J. P., KOSLOFF, R., and KOCH, C. P., “Protecting coherence in optimal control theory: State-dependent constraint approach,” *Physical Review A - Atomic, Molecular, and Optical Physics*, vol. 77, 2008.
- [70] KOSLOFF, R., RICE, S. A., GASPARD, P., TERSIGNI, S., and TANNOR, D. J., “Wavepacket dancing: Achieving chemical selectivity by shaping light pulses,” *Chemical Physics*, vol. 139, pp. 201–220, 1989.
- [71] SHI, S. and RABITZ, H., “Quantum mechanical optimal control of physical observables in microsystems,” *The Journal of Chemical Physics*, vol. 92, pp. 364–376, 1990.
- [72] PERKO, L., *Differential equations and dynamical systems*. Texts in applied mathematics, New York, Berlin, Heidelberg: Springer, 2001.
- [73] PALAO, J. P. and KOSLOFF, R., “Optimal control theory for unitary transformations,” *Physical Review A - Atomic, Molecular, and Optical Physics*, vol. 68, pp. 062308/1–062308/13, 2003.
- [74] MACHNES, S., SANDER, U., GLASER, S. J., DE FOUQUIERES, P., GRUSLYS, A., SCHIRMER, S., and SCHULTE-HERBRIGGEN, T., “Comparing, optimizing, and benchmarking quantum-control algorithms in a unifying programming framework,” *Physical Review A - Atomic, Molecular, and Optical Physics*, vol. 84, 2011.
- [75] SCHIRMER, S. G. and DE FOUQUIERES, P., “Efficient algorithms for optimal control of quantum dynamics: The krotov method unencumbered,” *New Journal of Physics*, vol. 13, 2011.
- [76] ZHU, W., BOTINA, J., and RABITZ, H., “Rapidly convergent iteration methods for quantum optimal control of population,” *Journal of Chemical Physics*, vol. 108, pp. 1953–1963, 1998.
- [77] ZHU, W. and RABITZ, H., “A rapid monotonically convergent iteration algorithm for quantum optimal control over the expectation value of a positive definite operator,” *Journal of Chemical Physics*, vol. 109, pp. 385–391, 1998.

- [78] MADAY, Y. and TURINICI, G., “New formulations of monotonically convergent quantum control algorithms,” *Journal of Chemical Physics*, vol. 118, pp. 8191–8196, 2003.
- [79] OHTSUKI, Y., TURINICI, G., and RABITZ, H., “Generalized monotonically convergent algorithms for solving quantum optimal control problems,” *Journal of Chemical Physics*, vol. 120, pp. 5509–5517, 2004.
- [80] DE FOUQUIERES, P., SCHIRMER, S. G., GLASER, S. J., and KUPROV, I., “Second order gradient ascent pulse engineering,” *Journal of Magnetic Resonance*, vol. 212, pp. 412–417, 2011.
- [81] CASTRO, A. and GROSS, E. K. U., “Acceleration of quantum optimal control theory algorithms with mixing strategies,” *Physical Review E - Statistical, Nonlinear, and Soft Matter Physics*, vol. 79, 2009.
- [82] KIRKPATRICK, S., GELATT JR., C. D., and VECCHI, M. P., “Optimization by simulated annealing,” *Science*, vol. 220, pp. 671–680, 1983.
- [83] ČERNÝ, V., “Thermodynamical approach to the traveling salesman problem: An efficient simulation algorithm,” *Journal of Optimization Theory and Applications*, vol. 45, pp. 41–51, 1985.
- [84] METROPOLIS, N., ROSENBLUTH, A. W., ROSENBLUTH, M. N., TELLER, A. H., and TELLER, E., “Equation of state calculations by fast computing machines,” *The Journal of Chemical Physics*, vol. 21, pp. 1087–1092, 1953.
- [85] PRESS, W. H., TEUKOLSKY, S. A., VETTERLING, W. T., and FLANNERY, B. P., *Numerical Recipes 3rd Edition: The Art of Scientific Computing*. New York, NY, USA: Cambridge University Press, 3 ed., 2007.
- [86] KIRKPATRICK, S., “Optimization by simulated annealing: Quantitative studies,” *Journal of Statistical Physics*, vol. 34, pp. 975–986, 1984.
- [87] HODGSON, T. E., VIOLA, L., and D’AMICO, I., “Towards optimized suppression of dephasing in systems subject to pulse timing constraints,” *Phys. Rev. A*, vol. 81, p. 062321, 2010.
- [88] HAYES, D., KHODJASTEH, K., VIOLA, L., and BIERCUK, M. J., “Reducing sequencing complexity in dynamical quantum error suppression by walsh modulation,” *Phys. Rev. A*, vol. 84, p. 062323, 2011.
- [89] COOPER, A., MAGESAN, E., YUM, H. N., and CAPPELLARO, P., “Time-resolved magnetic sensing with electronic spins in diamond,” *Nature Communications*, vol. 5, 2014.
- [90] BALL, H. and BIERCUK, M. J., “Walsh-synthesized noise-filtering quantum logic,” *arXiv:quant-ph/1410.1624*, 2014.

- [91] RADEMACHER, H., “Einige stze ber reihen von allgemeinen orthogonalfunktionen,” *Mathematische Annalen*, vol. 87, pp. 112–138, 1922.
- [92] CUMMINS, H. K., LLEWELLYN, G., and JONES, J. A., “Tackling systematic errors in quantum logic gates with composite rotations,” *Phys. Rev. A*, vol. 67, p. 042308, 2003.
- [93] JONES, J. A., “Designing short robust not gates for quantum computation,” *Phys. Rev. A*, vol. 87, p. 052317, 2013.
- [94] WEISSMAN, M. B., “ $\frac{1}{f}$ noise and other slow, nonexponential kinetics in condensed matter,” *Rev. Mod. Phys.*, vol. 60, pp. 537–571, 1988.
- [95] PALADINO, E., FAORO, L., FALCI, G., and FAZIO, R., “Decoherence and $1/f$ noise in josephson qubits,” *Phys. Rev. Lett.*, vol. 88, p. 228304, 2002.
- [96] FAORO, L. and VIOLA, L., “Dynamical suppression of $1/f$ noise processes in qubit systems,” *Phys. Rev. Lett.*, vol. 92, p. 117905, 2004.
- [97] HARRIS, F. J., “On the use of windows for harmonic analysis with the discrete fourier transform,” *Proceedings of the IEEE*, vol. 66, pp. 51–83, 1978.
- [98] THOM, J., WILPERS, G., RIIS, E., and SINCLAIR, A. G., “Accurate and agile digital control of optical phase, amplitude and frequency for coherent atomic manipulation of atomic systems,” *Optics Express*, vol. 21, pp. 18712–18723, 2013.
- [99] SENGUPTA, P. and PRYADKO, L. P., “Scalable design of tailored soft pulses for coherent control,” *Physical Review Letters*, vol. 95, 2005.
- [100] WALSH, J. L., “A closed set of normal orthogonal functions,” *American Journal of Mathematics*, vol. 45, pp. pp. 5–24, 1923.
- [101] JOHANSSON, J. R., NATION, P. D., and NORI, F., “Qutip 2: A python framework for the dynamics of open quantum systems,” *Computer Physics Communications*, vol. 184, pp. 1234 – 1240, 2013.
- [102] JOHANSSON, J. R., NATION, P. D., and NORI, F., “Qutip: An open-source python framework for the dynamics of open quantum systems,” *Computer Physics Communications*, vol. 183, pp. 1760 – 1772, 2012.
- [103] LANGER, C., OZERI, R., JOST, J. D., CHIAVERINI, J., DEMARCO, B., BEN-KISH, A., BLAKESTAD, R. B., BRITTON, J., HUME, D. B., ITANO, W. M., LEIBFRIED, D., REICHLE, R., ROSEN BAND, T., SCHAE TZ, T., SCHMIDT, P. O., and WINELAND, D. J., “Long-lived qubit memory using atomic ions,” *Physical Review Letters*, vol. 95, 2005.
- [104] NOEK, R., VRIJSEN, G., GAULTNEY, D., MOUNT, E., KIM, T., MAUNZ, P., and KIM, J., “High speed, high fidelity detection of an atomic hyperfine qubit,” *Optics Letters*, vol. 38, pp. 4735–4738, 2013.

- [105] HOME, J. P., HANNEKE, D., JOST, J. D., AMINI, J. M., LEIBFRIED, D., and WINELAND, D. J., “Complete methods set for scalable ion trap quantum information processing,” *Science*, vol. 325, pp. 1227–1230, 2009.
- [106] BROWN, K. R., WILSON, A. C., COLOMBE, Y., OSPELKAUS, C., MEIER, A. M., KNILL, E., LEIBFRIED, D., and WINELAND, D. J., “Single-qubit-gate error below 10^{-4} in a trapped ion,” *Physical Review A - Atomic, Molecular, and Optical Physics*, vol. 84, 2011.
- [107] HARTY, T. P., ALLCOCK, D. T. C., BALLANCE, C. J., GUIDONI, L., JANACEK, H. A., LINKE, N. M., STACEY, D. N., and LUCAS, D. M., “High-fidelity preparation, gates, memory, and readout of a trapped-ion quantum bit,” *Physical Review Letters*, vol. 113, 2014.
- [108] KNILL, E., LEIBFRIED, D., REICHLE, R., BRITTON, J., BLAKESTAD, R. B., JOST, J. D., LANGER, C., OZERI, R., SEIDELIN, S., and WINELAND, D. J., “Randomized benchmarking of quantum gates,” *Physical Review A - Atomic, Molecular, and Optical Physics*, vol. 77, 2008.
- [109] BENHELM, J., KIRCHMAIR, G., ROOS, C. F., and BLATT, R., “Towards fault-tolerant quantum computing with trapped ions,” *Nature Physics*, vol. 4, pp. 463–466, 2008.
- [110] BALLANCE, C. J., HARTY, T. P., LINKE, N. M., and LUCAS, D. M., “High-fidelity two-qubit quantum logic gates using trapped calcium-43 ions,” *arXiv:quant-ph/1406.5473*, 2015.
- [111] WALLMAN, J. J. and FLAMMIA, S. T., “Randomized benchmarking with confidence,” *New Journal of Physics*, vol. 16, 2014.
- [112] MAGESAN, E., GAMBETTA, J. M., and EMERSON, J., “Characterizing quantum gates via randomized benchmarking,” *Physical Review A - Atomic, Molecular, and Optical Physics*, vol. 85, 2012.
- [113] CHIAVERINI, J., BLAKESTAD, R. B., BRITTON, J., JOST, J. D., LANGER, C., LEIBFRIED, D., OZERI, R., and WINELAND, D. J., “Surface-electrode architecture for ion-trap quantum information processing,” *Quantum Information and Computation*, vol. 5, pp. 419–439, 2005.
- [114] KIM, J., PAU, S., MA, Z., MCLELLAN, H. R., GATES, J. V., KORNBLIT, A., SLUSHER, R. E., JOPSON, R. M., KANG, I., and DINU, M., “System design for large-scale ion trap quantum information processor,” *Quantum Information and Computation*, vol. 5, pp. 515–537, 2005.
- [115] MOUNT, E., BAEK, S. Y., BLAIN, M., STICK, D., GAULTNEY, D., CRAIN, S., NOEK, R., KIM, T., MAUNZ, P., and KIM, J., “Single qubit manipulation in a microfabricated surface electrode ion trap,” *New Journal of Physics*, vol. 15, 2013.

- [116] HAYES, D., MATSUKEVICH, D. N., MAUNZ, P., HUCUL, D., QURAISHI, Q., OLMSCHENK, S., CAMPBELL, W., MIZRAHI, J., SENKO, C., and MONROE, C., “Entanglement of atomic qubits using an optical frequency comb,” *Physical Review Letters*, vol. 104, 2010.
- [117] EMERSON, J., ALICKI, R., and ZYCKOWSKI, K., “Scalable noise estimation with random unitary operators,” *Journal of Optics B: Quantum and Semiclassical Optics*, vol. 7, pp. S347–S352, 2005.